

Eddy resolving strategies in turbomachinery and peripheral components

Tucker, P. G.; Wang, Z. N.

DOI:

[10.1115/1.4048697](https://doi.org/10.1115/1.4048697)

License:

Creative Commons: Attribution (CC BY)

Document Version

Peer reviewed version

Citation for published version (Harvard):

Tucker, PG & Wang, ZN 2021, 'Eddy resolving strategies in turbomachinery and peripheral components', *Journal of Turbomachinery*, vol. 143, no. 1, 010801. <https://doi.org/10.1115/1.4048697>

[Link to publication on Research at Birmingham portal](#)

Publisher Rights Statement:

ASME ©; CC-BY distribution license

General rights

Unless a licence is specified above, all rights (including copyright and moral rights) in this document are retained by the authors and/or the copyright holders. The express permission of the copyright holder must be obtained for any use of this material other than for purposes permitted by law.

- Users may freely distribute the URL that is used to identify this publication.
- Users may download and/or print one copy of the publication from the University of Birmingham research portal for the purpose of private study or non-commercial research.
- User may use extracts from the document in line with the concept of 'fair dealing' under the Copyright, Designs and Patents Act 1988 (?)
- Users may not further distribute the material nor use it for the purposes of commercial gain.

Where a licence is displayed above, please note the terms and conditions of the licence govern your use of this document.

When citing, please reference the published version.

Take down policy

While the University of Birmingham exercises care and attention in making items available there are rare occasions when an item has been uploaded in error or has been deemed to be commercially or otherwise sensitive.

If you believe that this is the case for this document, please contact UBIRA@lists.bham.ac.uk providing details and we will remove access to the work immediately and investigate.



ASME Accepted Manuscript Repository

Institutional Repository Cover Sheet

First

Last

ASME Paper Title: Eddy resolving strategies in turbomachinery and peripheral components

Authors: P. G. Tucker, Z. N. Wang

ASME Journal Title: Journal of Turbomachinery

Volume/Issue: Volume 143, Issue 1

Date of Publication (VOR* Online): December 28, 2020

ASME Digital Collection URL: <https://asmedigitalcollection.asme.org/turbomachinery/article-abstract/143/1/01080>: Resolving-Strategies-in-Turbomachinery-and?redirectedFrom=fulltext

DOI: 10.1115/1.4048697

*VOR (version of record)

Eddy Resolving Strategies in Turbomachinery and Peripheral Components

P. G. Tucker and Z. N. Wang

The University of Cambridge
Department of Engineering
Cambridge
CB2 1PZ, United Kingdom

Summary

The successful application of eddy resolving simulations to most areas of a modern gas turbine aeroengine is considered. A coherent modelling framework is presented to address coupling challenges. A flow classification is also given. The extensive results presented are shown to be promising but many challenges remain. In the short term, the use of eddy resolving simulations should see greater use in RANS (Reynolds Averaged Navier-Stokes) and lower order model calibration/development – this is starting to happen already. Ideally, in the near future, RANS, LES (Large Eddy Simulation) & test should work in harmony. It is advocated that currently, certain costly engineering design problems can be avoided or understood using scale resolving simulations.

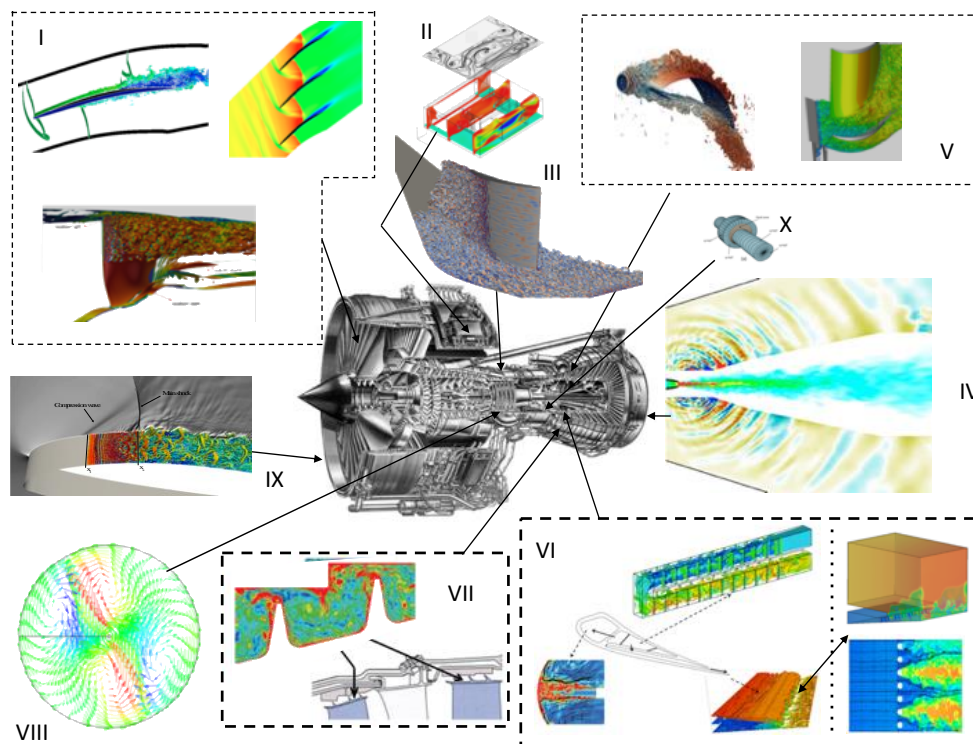


Figure 1. Engine zones where eddy resolving simulations performed (adapted from Tucker [1] - Published with the kind permission of Springer): (I) Transonic fan; (II) electronics/avionics system; (III) compressor flow; (IV) propulsive jet; (V) low-pressure turbine flows; (VI) cooling flows; (VII) labyrinth seals; (VIII) high-pressure compressor drum; (IX) nacelle lip line and (X) hydrodynamic journal bearing.

Introduction

This paper largely recalls a groups experience of using unsteady/eddy resolving simulations to predict the flow in different components of gas turbine engines. The wide range of areas considered are identified in Figure 1. The gas turbine is intrinsically a coupled system. For example, at its most basic coupling level, the system consists of rows of rotating and stationary blade row pairs. Balancing the general requirement for computationally expensive large-scale simulations combined with already computationally expensive eddy resolving simulations seems in its infancy with very few examples (see, for example, de Laborderie et al. [2,3,4] who apply AVBP codes with over a billion cells to a 3.5 stage high pressure compressor). Nonetheless some thoughts on this aspect, as well as dealing with the individual components is offered. The main focus of this work has been performing meaningful eddy resolving simulations for jet engine components at minimal cost while paying attention to this coupling challenge through hierarchical simulations.

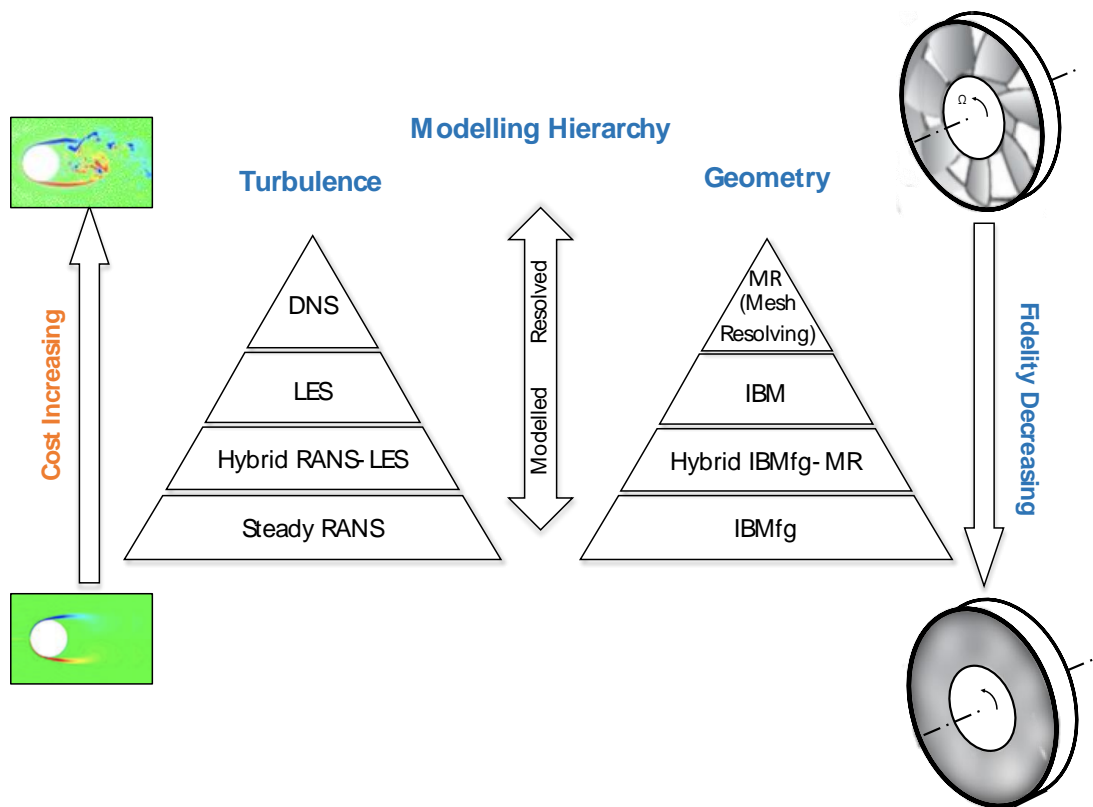


Figure 2. Hierarchy of modelling geometry and turbulence.

Scale Resolving

As shown in Figure 2 it is postulated that there is a hierarchy for modelling geometry and turbulence. For turbulence the hierarchy goes from RANS to DNS (Direct Numerical Simulation) i.e. fully filtered to fully resolved. For geometry, the geometry can be fully resolved on the mesh - MR. Typically, through body forces, IBM (Immersed Boundary Method) can then be used. At the RANS analogous end of the geometry modelling spectrum is IBMfg – IBM with filtered geometry. With respect to a fan this looks as shown in the Figure 2, right-hand side, the lower image. This shows the geometry azimuthally filtered. This is largely achieved using an IBM method with circumferentially homogenous forces to turn the

flow to the blade's camberline (see Cao et al. [5]). The approach can be used as an economical means of including coupling. For example, a mesh resolved blade row could be sandwiched between IBMfg modelled rows giving a hybrid simulation. Loss can be modelled globally (in a particular blade row) or locally to approximately generate wakes. For, example, global IBMfg could be used to get capture the general system behaviour of a fan. Localized forces could be used to generate wakes to feed into downstream components. Body forces/IBM is also useful for more peripheral purposes. These will be outlined later.

Resolution Requirements

Figure 3, adapted from Tucker et al. [6], extends that of Mayle [7] for a medium-sized gas turbine engine. The extension involves adding LES grid requirements. Mayle plotted the Reynolds number through a gas turbine engine. The dashed line gives this Reynolds number (see right hand axis label). The red line with symbols shows the wall resolved LES grid requirements, where the grid is fine enough to avoid the need for modelling. The blue line with triangle symbols gives the Wall Modelled LES (WMLES) or Zonal LES (ZLES) requirements. With this some form of RANS or RANS related modelling is used near walls. The purple line gives an estimate of the grid requirements if a high order discretization is used with wall resolved LES. Looking at the graph, it would seem that, except for the Low-Pressure Turbine (LPT), on the grounds of reasonable costs, WMLES seems sensible. However, the grey scale identifies the Reynolds number range where there is transition to turbulence. The data used, to set the grey scale, is for compressor blades. However, any uncertainty in applying these estimates to other zones does not affect the points to be made. Firstly, it is clear the fan flow is turbulent (it is in the white region of the graph) and hence amenable to WMLES. However, some compressor stages can be transitional (falling in the grey zone), needing wall resolved LES tending to quasi-DNS (Direct Numerical Simulation – where all the turbulent scales are resolved) to deal with the transition. The LPT has such a low Reynolds number that the WMLES and wall resolved LES costs are comparable and hence wall resolved LES comfortable. The propulsive jet nozzle clearly needs WMLES or some form of hybrid RANS-LES modelling. It should be stressed that the estimates given in the figure (for blade flows) are just for the air foil boundary layer of a single blade. Hence, there is no wake, hub or shroud flow resolution. Therefore, care is needed to avoid underestimating grid costs when using Figure 3. Note, the purple line shows the exciting potential of high-order methods and hence the re-emergence of interest in such approaches in many applications including turbomachinery [8,9,10,11,12].

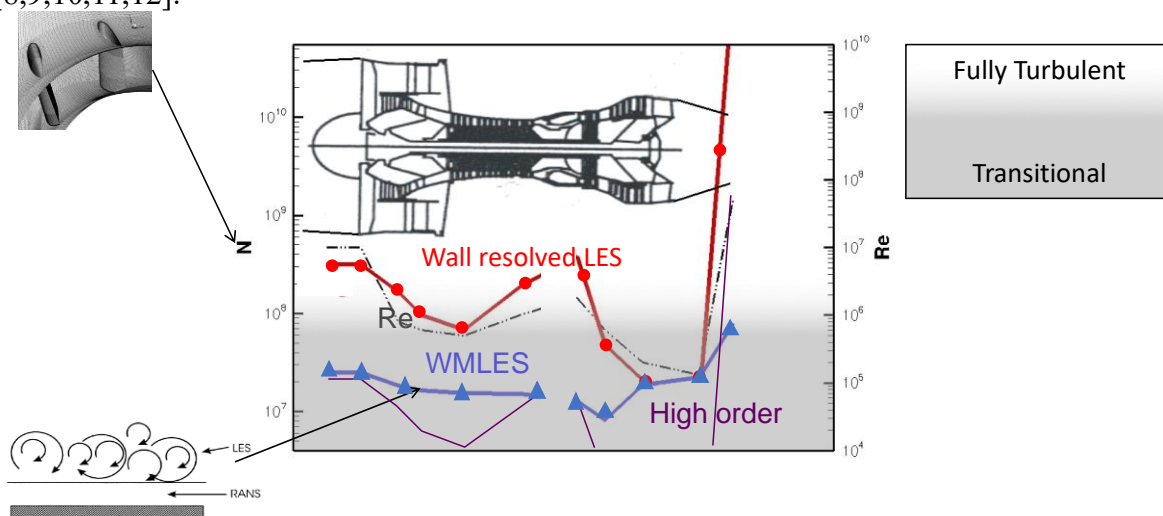


Figure 3. Resolution requirements (Adapted from Tucker et al. [6]).

Flow Classification

Figure 4 gives an approximate flow classification for turbomachinery. The first column relates to Class A flows. These are predominantly Reynolds number independent, wake type flows. These include ribbed passages (as found inside high pressure turbine blades), cut back trailing edges - CBTE (see later), propulsive jets and avionics. The latter are populated by rows of integrated circuits. Next there are Class (B), low Reynolds number flows. The Reynolds numbers are moderate enough that LES (or Implicit LES – ILES) can be exploited with tolerable grid densities. Such systems potentially include low pressure turbine blades, some high-pressure compressor drum conditions, intakes in crosswinds and hydrodynamic journal bearings. Note, the latter are just used in land-based turbines. With regards to the high-pressure compressor drum the core flow involves an unsteady system that rotates within around 10% of the cavity angular velocity. At the inner cavity radius there can (depending on the configuration) be high Reynolds number elements.

Class (C) relates to flows where the Reynolds number is high enough to make LES challenging. However, the boundary layer flow also has complex transitional elements. This makes wall resolved LES or DNS essential and the combination of this with the substantial Reynolds number makes simulations expensive.

Class (D) flows are high Reynolds number, where one would like to exploit hybrid RANS-LES or perhaps WMLES. However, this approach will be limited in effectivity. For example, with the HPT (High Pressure Turbine), the surface is populated by numerous cooling holes and the RANS layer will potentially disrupt this. For the convoluted intake duct and intake during climb, the RANS layer will exert a critical, uncertain, control of the separation point. The labyrinth and rim seals (2nd and 3rd items in Column (D)) are mixed flows. They have a substantial Class (A) flow element. However, their surfaces move at high velocity into the page giving a high Reynolds number boundary layer.

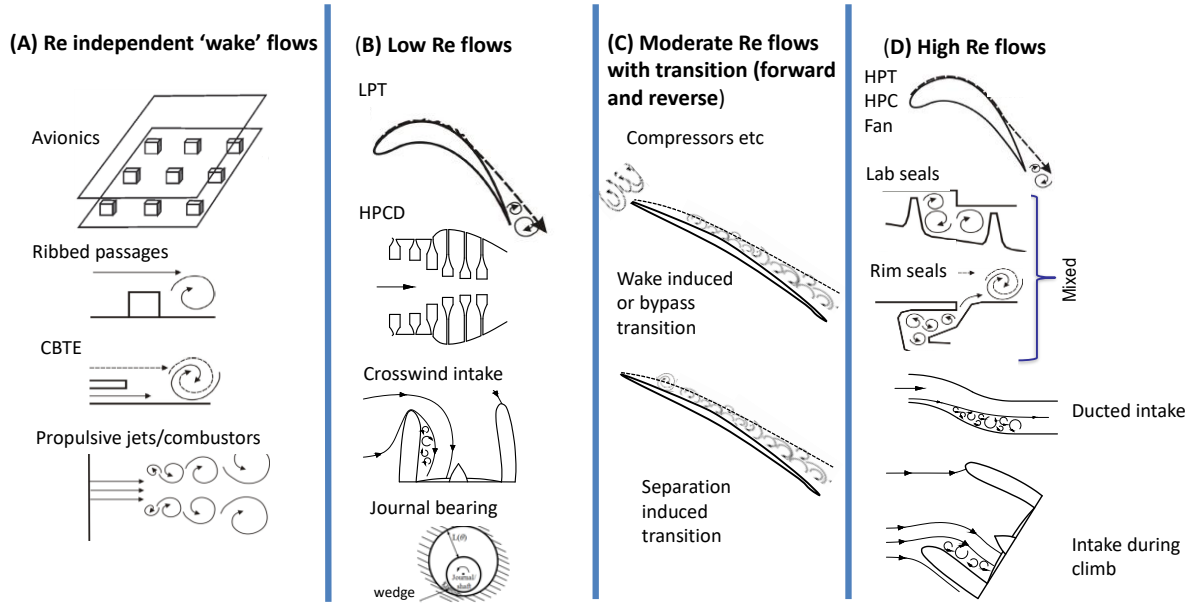


Figure 4. Flow classification.

Next we will work our way through the engine looking at the different classes of flow just noted and applying, where expedient, hybridizations of both geometry and turbulence.

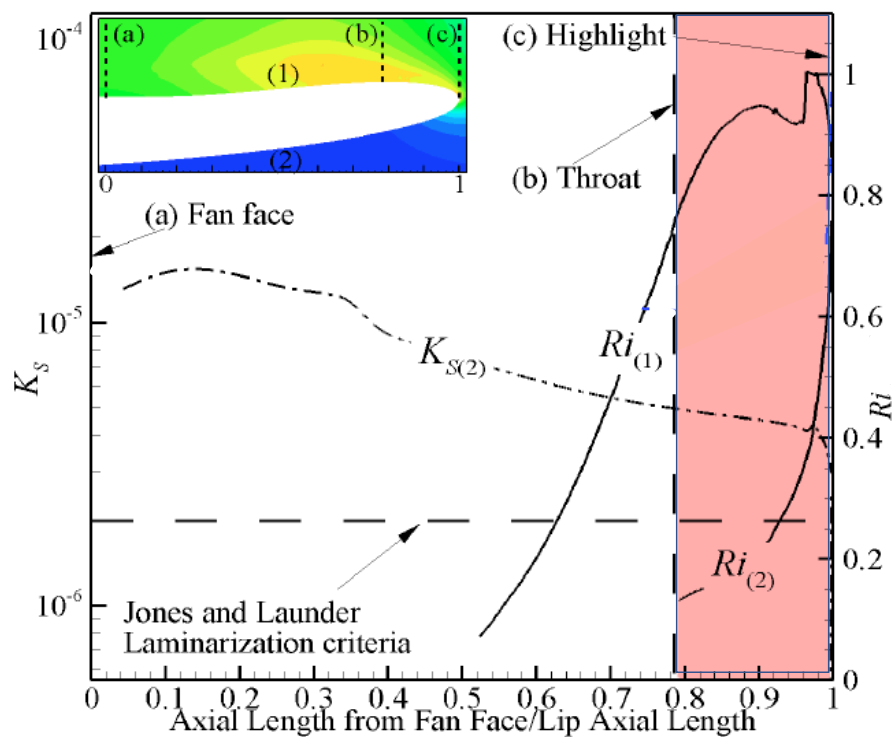


Figure 5. Variation of acceleration parameter, K_S , and Richardson number, Ri , around and intake lip in a crosswind (from Oriji et al. [13]).

Numerical Approach

Unless stated otherwise the code used is the Rolls-Royce CFD code Hydra (Crompton et al [14]). It is a second-order unstructured, mixed element, density based, finite-volume code. Temporal discretization is performed with a standard five-stage Runge–Kutta algorithm. To improve the code’s performance at low Mach numbers, the code has been modified to evaluate the pressure using an artificial compressibility method (Rogers et al. [15]). For ZLES calculations, unless otherwise state, for $y^+ < 60$ the SA (Spalart and Allmaras [16]) model is used. Outside this RANS zone either LES is used or Implicit LES. A schematic of the process can be seen in the lower left hand insert of Figure 3. The alternative code used in this work is NEAT (Tucker [17]). This is a structured, staggered grid, pressure based, implicit flow solver with a range of LES models and Crank-Nicolson time advancement.

Results

Note, for brevity, since a wide range of cases are considered, only brief case setup details are given. However, full details can be found in the cited references for each case.

Intakes

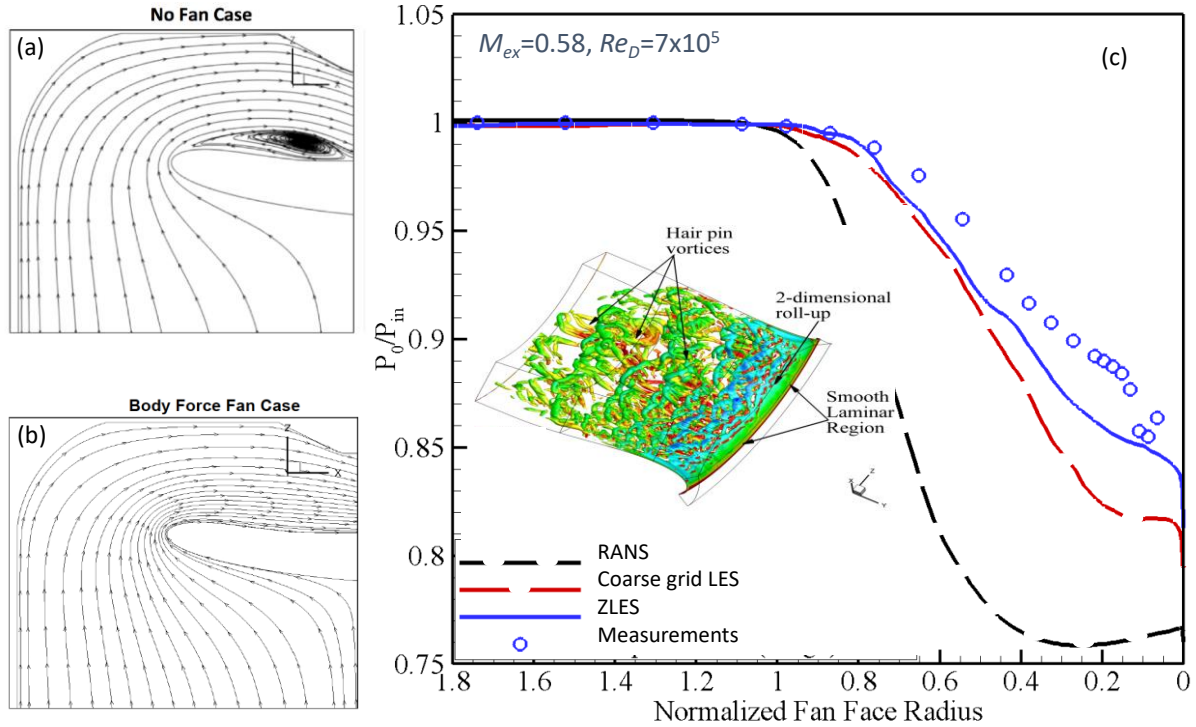


Figure 6 Intake in crosswind (adapted from Oriji [13]).

Intake in Cross Wind. First we will look at an intake when the aircraft is notionally on the runway and subjected to crosswinds. In relation to this, Figure 5 shows the distribution of acceleration parameter (K_s) and curvature related Richardson number (Ri), where 1, on the x -axis, corresponds to the highlight and 0 the fan face (see Figure 5 insert). The subscripts (1) and (2) in Figure 5 are used to indicate whether the interior or exterior part of the intake is being considered. As can be seen, there are extreme and complex variations of K_s and Ri . The high K_s and Ri gives rise to the potential for flow laminarization and hence flow separation. These things make this a Class B flow (see later).

Figure 6 shows results when replicating a rig designed to capture an aircraft engine in crosswinds. Full details of the numerical (and to an extent experimental) setup can be found in Oriji [18]. The streamlines for a case without and with a fan modelled are shown in Frames (a) and (b), respectively. As noted, the crosswind flow around the lip of an intake is complex and there is acceleration (see Frame (a)) severe enough to laminarize the boundary layer. Similarly, as noted, the curvature around the lip is sufficient to laminarize the flow. The laminarized flow meets a shock, the combined effect of these are expected to induce early separation, subsequent separated flow transition and ultimately distortion at the fan face. Another complexity is that the fan's demand for airflow can help clean up the separation (assuming that the separation does not give rise to fan instability). In Frame (b), the separation has been suppressed by the fan modelled using IBMfg. In frame (c) the total pressure at the notional fan face is plotted. Consistent with the experiment there is no fan in the simulation. Although it is easy in the simulation, through use of the IBMfg model, it is expensive replicate

a fan in a rig. The symbols in Figure 6 are the measurements. The black short dashed line, showing poor agreement with the measurements, is the result for the SA RANS model. The blue full line is for a ZLES and the red long dashed line for an LES¹. The latter, considering the systems Reynolds number ($Re = 7 \times 10^5$ with an exit Mach number of around 0.6) would seem too coarse for an LES using just 33 million cells. However, rather than basing the Reynolds number length scale on the intake diameter it would be more realistic to base the Reynolds number on the boundary layer thickness around the lip and this, after being subjected to extreme acceleration with streamline curvature, is thin. Hence, the true system Reynolds number is relatively modest. Therefore, the coarse grid LES gives a credible performance even on a modest grid – this is encouraging for wall resolved LES. Nonetheless, for this coarse grid some form of wall modelling has proved helpful. To gain useful results for engine design, the fan should ideally be included. As noted, for measurements, this is expensive needing the installation of a fan and a drive system etc.

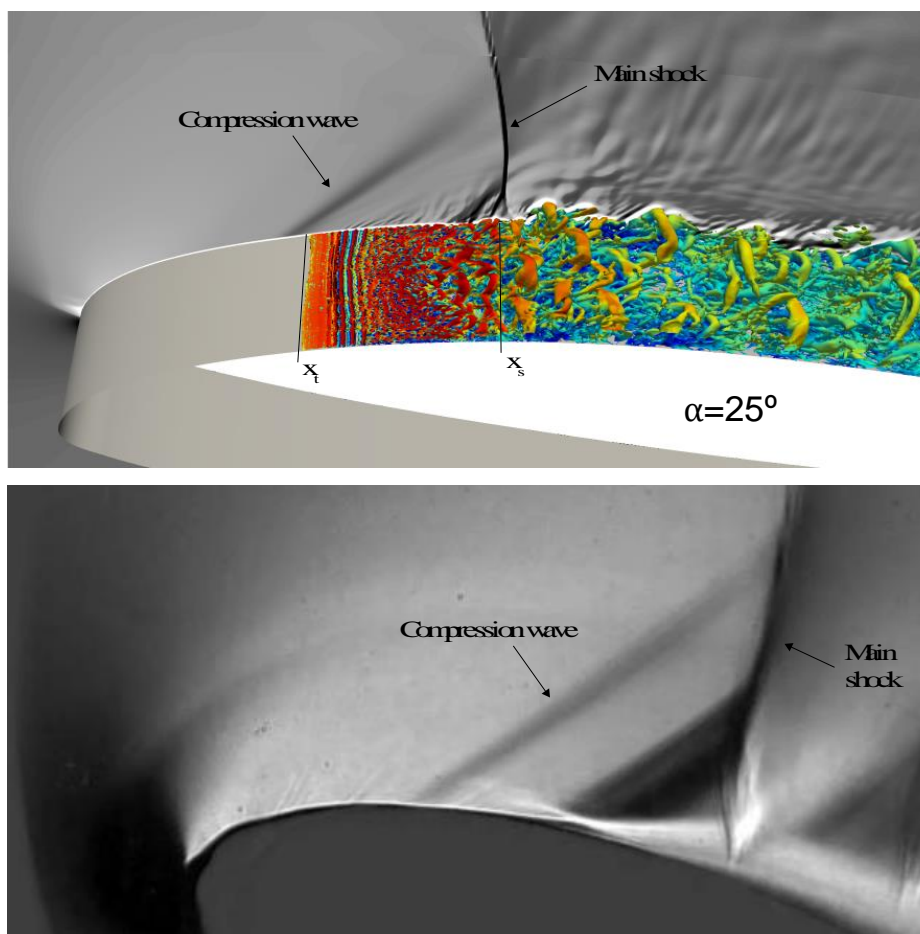


Figure 7. Schlieren imaging with Q criterion coloured by velocity.

Intake During Climb. Next we will look at comparisons with measurements from a rig intended to replicate the intake lip flow physics during climb – a Class D flow. Again, it would be easy to numerically model the impact of a fan. However, since this was not, due to difficulties/expense etc., done in the experiments neither is this done numerically. Comparison is made for an angle of attack $\alpha = 25^\circ$, $M \approx 0.4$ (Mach number of flow approaching the

¹ Note in all simulations the LES branch is Implicit LES

lip) and $Re \approx 5 \times 10^5$ (based on the lip thickness, L). ZLES is performed with approximately 14 million grid points and wall resolved LES with 50 million grid points. Full test case details can be found in Kalsi and Tucker [189]. Figure 7 shows Schlieren imaging. The lower frame gives experimental imaging and the upper the equivalent for the CFD based around contouring the density gradient (with the Q criterion coloured by velocity also included). In both images the main shock and compression wave are evident.

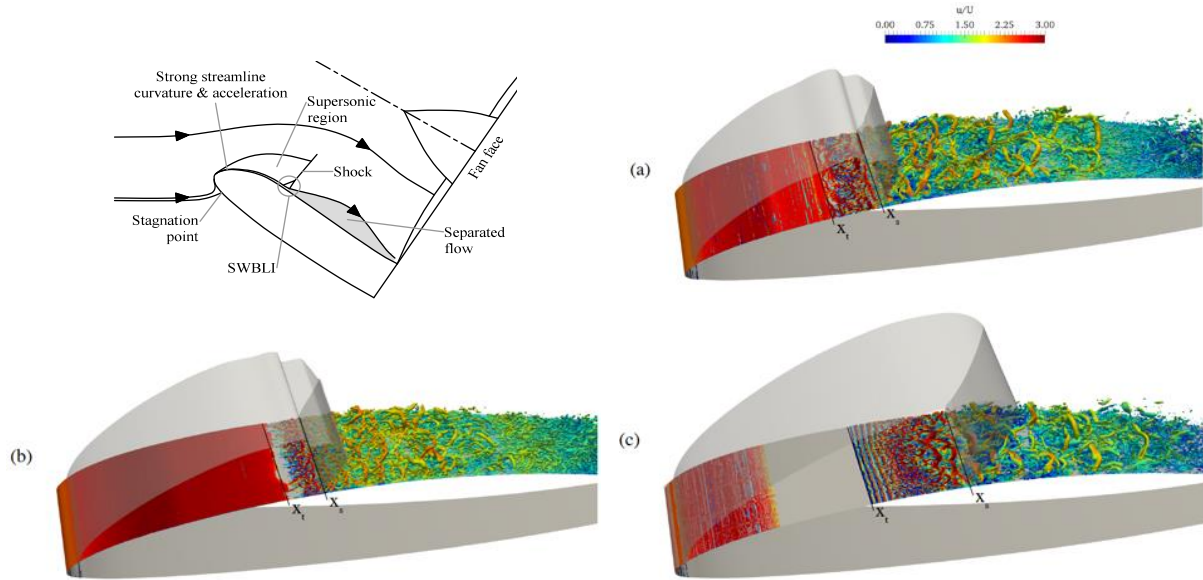


Figure 8. Temporal variation of flow transition (from Kalsi [20]) – Q criterion coloured by velocity, grey isosurface ($M = 1$) shows the boundary of the supersonic region.

In Figure 8 lines marked x_t are used to identify the onset turbulence transition at this rig scale Reynolds number. As can be seen, the transition location is extremely unsteady. The grey $M = 1$ isosurface shows the boundary of the supersonic region. The line labelled x_s gives the shock location. Again, this is extremely unsteady and this unsteadiness along with that for the transition location clearly presents a strong challenge for RANS.

Figure 9 plots the inner lip static pressure coefficient variation with distance along the lip. C_p distributions display a sharp decrease at the leading edge of the upper aerofoil surface. This is as a result of the severe flow acceleration over the lip. The C_p plateaus under the supersonic region, before abruptly recovering under the shock at $dS \approx 1L$. This displays the severe adverse pressure gradient experienced by the boundary layer in the shock foot region. The observed distributions are typical of transonic flows. All CFD methods are able to capture this distribution well, although the standard RANS-SA model (black line) predicts shock location $0.1L$ upstream compared to experimental measurements. A modified SA model altered to account for the effects of acceleration and curvature (labelled Modified RANS) given by the dashed line, provides a noticeable improvement to this, moving the shock further downstream, agreeing well with experimental measurements and ZLES. Frame (b) of Figure 9 shows time averaged velocity profiles normal to the intake lip downstream of the shock. The flow here is significantly distorted, featuring large, unsteady, three-dimensional vortical structures. Hence,

RANS does not agree well with measurements. ZLES, on the other hand, is able to give a much better prediction of the post shock wave boundary layer interaction flow suggesting it is adequate for capturing the complex transitional flow physics associated with intakes during climb.

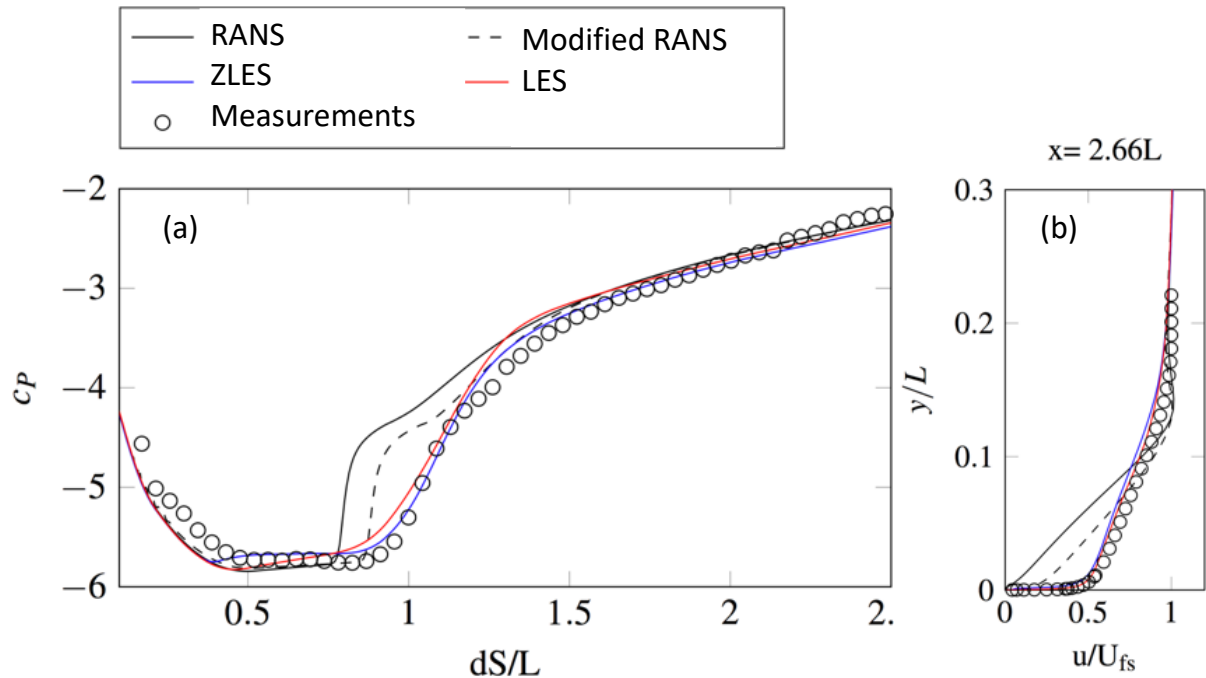


Figure 9. Quantitatively comparisons with measurements for intake during climb: (a) Static pressure coefficient and (b) Velocity profile (from Kalsi and Tucker [19]).

Fan Flow with Mixed Fidelity Modelling

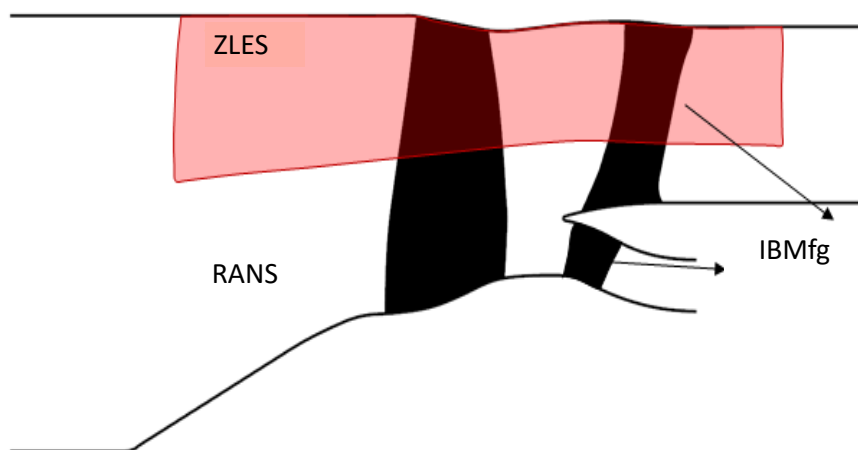


Figure 10. Schematic of fan geometry and hybrid geometry and turbulence modelling.

As the bypass ratio increases, the fan is becoming a key contributor to aeroengine landing noise. This noise is composed of tonal and broadband components. Fan tonal noise has been successfully suppressed, which makes the broadband components stand out. Broadband noise is closely related to turbulence of fan wakes and its interactions with downstream stators. The understanding of its generation mechanisms is still incomplete. At the approach condition of the fan considered here, the Reynolds number is around 3×10^6 . For this Class D flow, this corresponds to a grid requirement of around 3 billion (see Figure 3) for a wall resolved LES. Hence, here to keep cost down, the system shown in Figure 10 (a fan with outlet guide vane and ISS) is treated in a highly zonal and hierarchical fashion. The approach is zonal because the inner 50% of the blade span is RANS modelled and the outer 50% treated using ZLES. It is hierarchical because the outlet guide vane and ISS are modelled using IBMfg i.e. their geometry is azimuthally filtered.

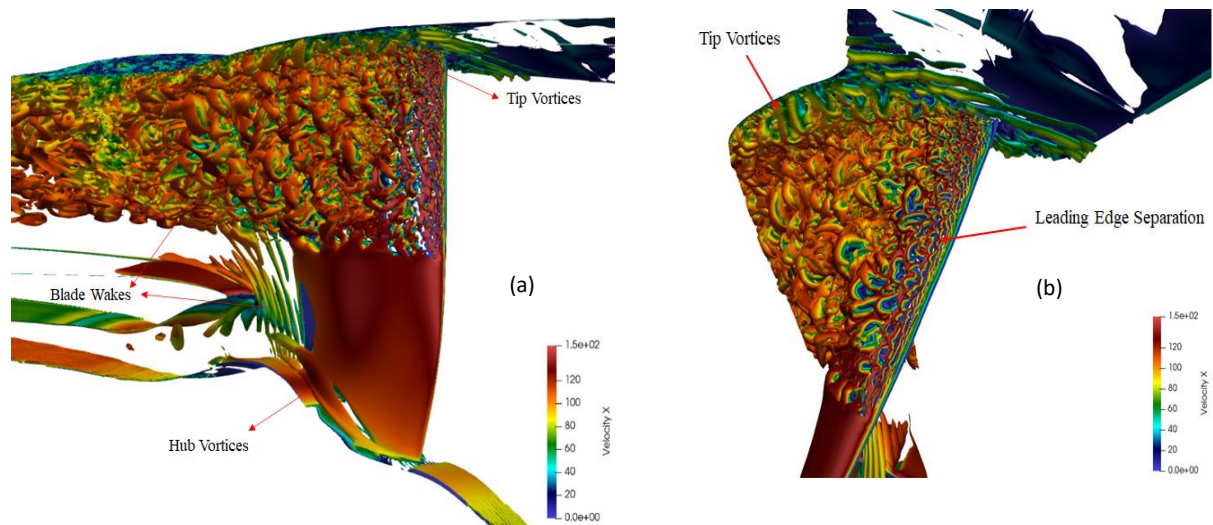


Figure 11. Instantaneous flow for a fan: (a) flow over full span and (b) focused view of tip region.

In Figure 11 the Q-criterion is used to show the flow structures. As shown in Frame (a), fine-scale turbulent structures are provided by ZLES from the tip to middle span, while ensemble averaged large-scale wake structures and a hub corner vortex (horse-shoe vortex) are revealed by RANS in the lower span. Frame (b) shows a close-up view of fan tip flow calculated using ZLES. The hair-pin vortices roll up near the leading edge and flow separation then occurs on the suction surface of the fan blade in the upper span. This is due to the positive flow incidence caused by the off-design rotational speed that is half of the design speed.

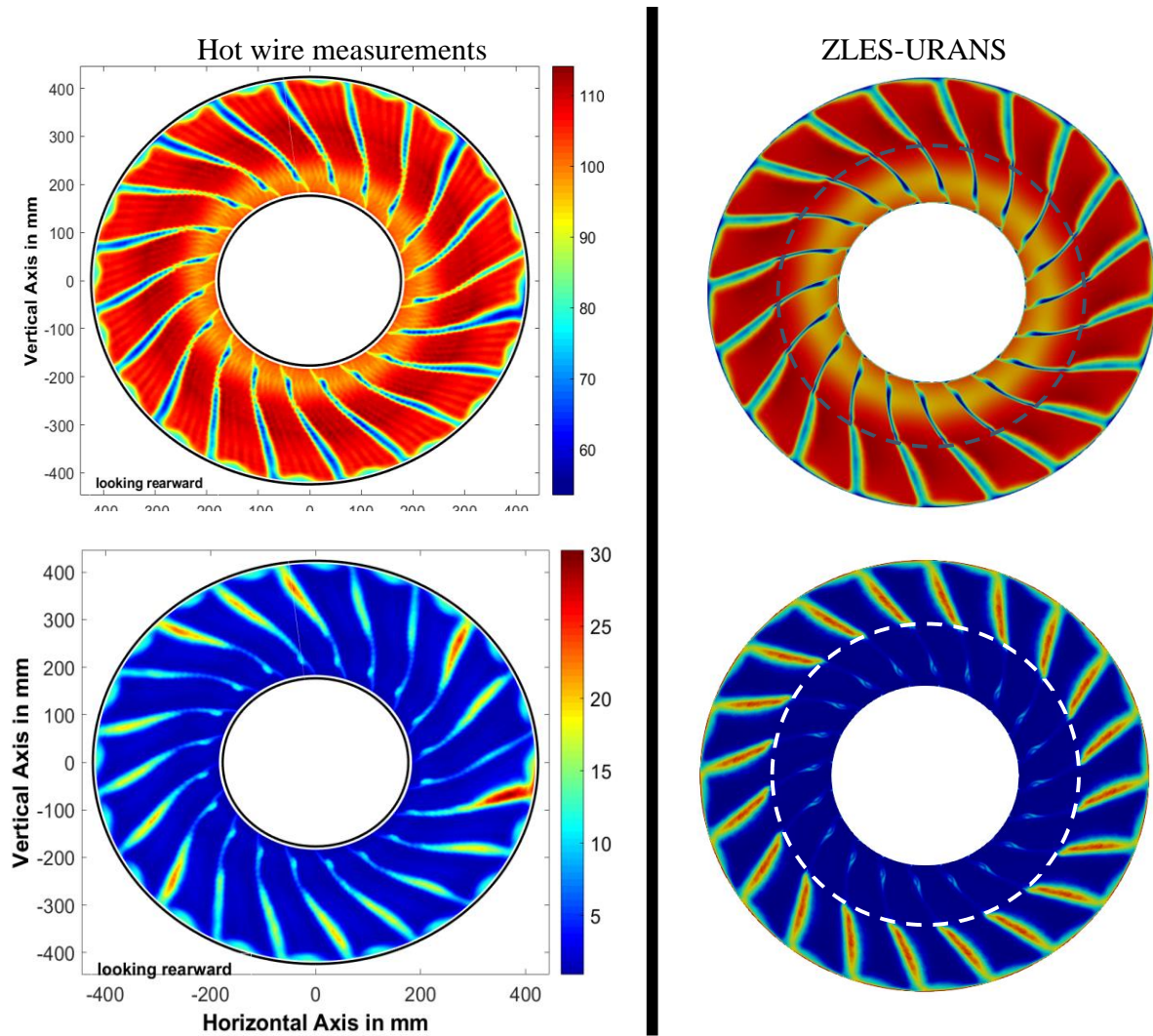


Figure 12. Comparison of time-averaged flow fields from the simulation with hot-wire measurements at a plane around 0.4 chords downstream of the rotor: upper frames velocity and lower frames turbulence intensity.

Figure 12 compares the time-averaged ZLES (with URANS) with hot-wire measurements at the plane around 0.4 chord downstream of the rotor. The left-hand column represents measurements. The right hand represents the simulations. The upper row gives axial velocity and the lower turbulence intensity. Azimuthal variations of axial velocity exist in the experiment, these could be physical, arising from fan blade vibration. In the simulation postprocessing, one blade passage is computed and duplicated to form a whole annulus. The same contours are used for comparisons. ZLES captures the fan suction surface separation and predicts a similar shape for the upper-span low velocity region. The lower frames show the axial velocity turbulent fluctuations from both the experiment and simulation. Although a large variation is seen in the experiment, the ZLES (with URANS component) captures the shape of some high turbulence regions. In the tip, the high turbulence and low velocity region is caused by tip vortices. Notably, the shape and size of the tip clearance vortex (and in particular its spanwise depth) are quite different in the simulations, when compared to data. Tests show the ZLES has minimal sensitivity to the thickness of the incoming boundary layer. However, the

designed tip clearance is used in the simulation. This is because the experiment had not been completed at the time that the simulation was made. A possible reason is that the tip clearance is larger in the experiment than used in the simulation. Exploring this is left as future work. However, overall, a qualitative agreement has been achieved between the simulation and experiment.

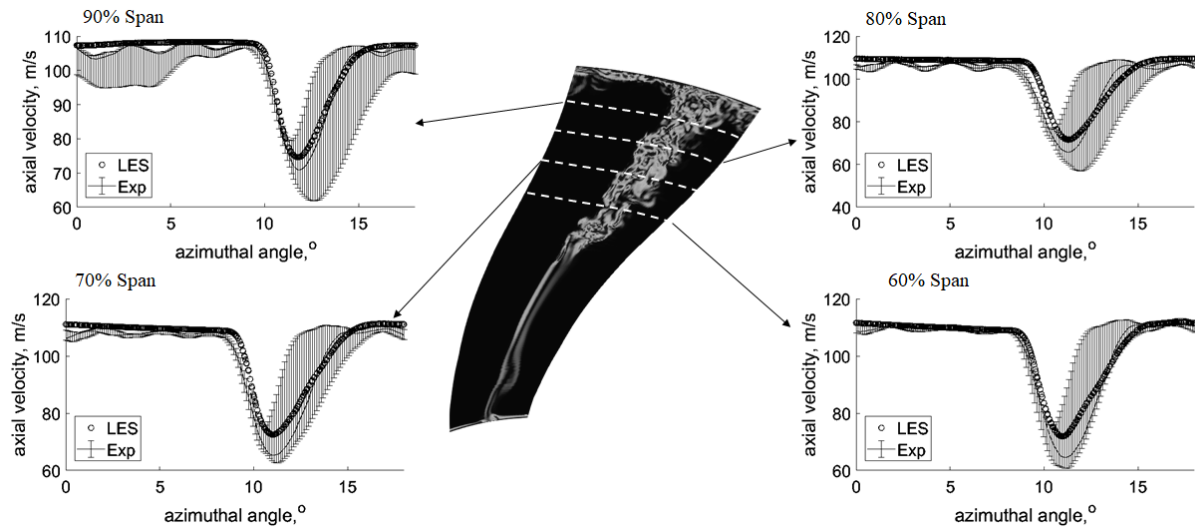


Figure 13. Wake profiles of axial velocity.

Figure 13 shows the quantitative comparison of axial velocity between ZLES and measurements in the wake region. The bars represent the variations across the passage. The wake from one passage is plotted using a full line, as a reference. The ZLES results are shown by red circles. The ZLES shows encouraging agreement with the wake profile in the reference passage and is within the variation across passages. The blade wake reaches a maximum width near 70% span. This is because of the separation on the suction surface. The hybrid hierarchical modelling approach of combining resolved geometry with filtered geometry and eddy resolving with RANS appears promising.

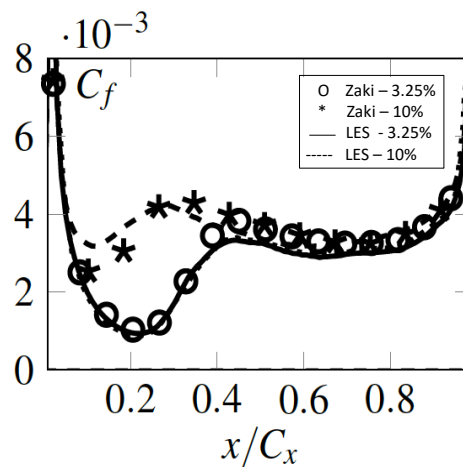


Figure 14. Time averaged skin friction coefficient on pressure surface of compressor blade (From Scillitoe [22]).

Compressor

Next we will consider a Class C flow, this being the flow over a compressor blade. Since this is a Class C flow, wall resolved LES is used.

Validation. Figure 14 gives pressure surface skin friction distributions. For low (3.25%) and high (10%) free-stream perturbations there is encouraging agreement with the DNS of Zaki et al. [21]. The level of agreement is similar for the suction surface (see Scillitoe et al. [22]).

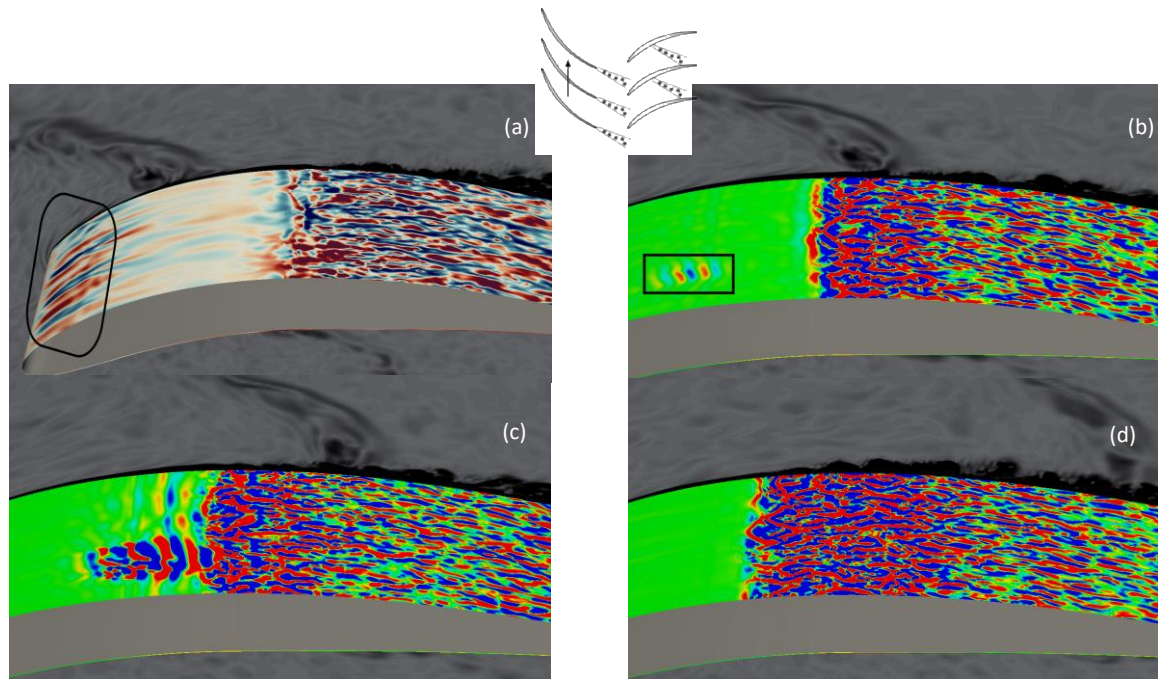


Figure 15. Flows at different wake passing phases at planes 15 wall units away from the suction surface.

Suction Surface Transition. Axial, core, turbomachinery typically consists of rows of rotating and stationary blades. Hence, such flows involve wakes. Therefore, next we will consider wake induced transition for a linear controlled diffusion aerofoil cascade (Gbadebo [23]) with $Re_c = 2.3 \times 10^5$. Notably the current simulations make use of the σ LES model (Nicoud et al. [24]) and this, with good quality grids, seems adequate at capturing a wide range of complex transition mechanisms that can be found in compressors (see Scillitoe et al. [22]). The results shown here are from Scillitoe et al. [22], having a free stream turbulence intensity of 1.5% and a grid of circa 10 million cells. Figure 15 shows flow snapshots at different wake passing phases. These snapshots are at planes 15 wall units away from the suction surface. Frame (a) shows contours of tangential velocity perturbations. These help reveal the wake amplified Klebanoff streaks (convecting at around 70% of the free stream velocity). The remaining frames give perturbations of normal velocity. These show that the Klebanoff streaks give rise to spots (Frames (b,c)) and the spots give rise to earlier transition – see Frame (d). Note, that the transition is separation induced. Blade loss depends on wake period. Therefore, it is clear that we must accurately capture the convection speed of streaks. None of the current RANS based transition models do this for this Class C flow.

The flow is clearly challenging and if such a transition mechanism takes place at real engine Reynolds numbers then this gives a severe challenge.

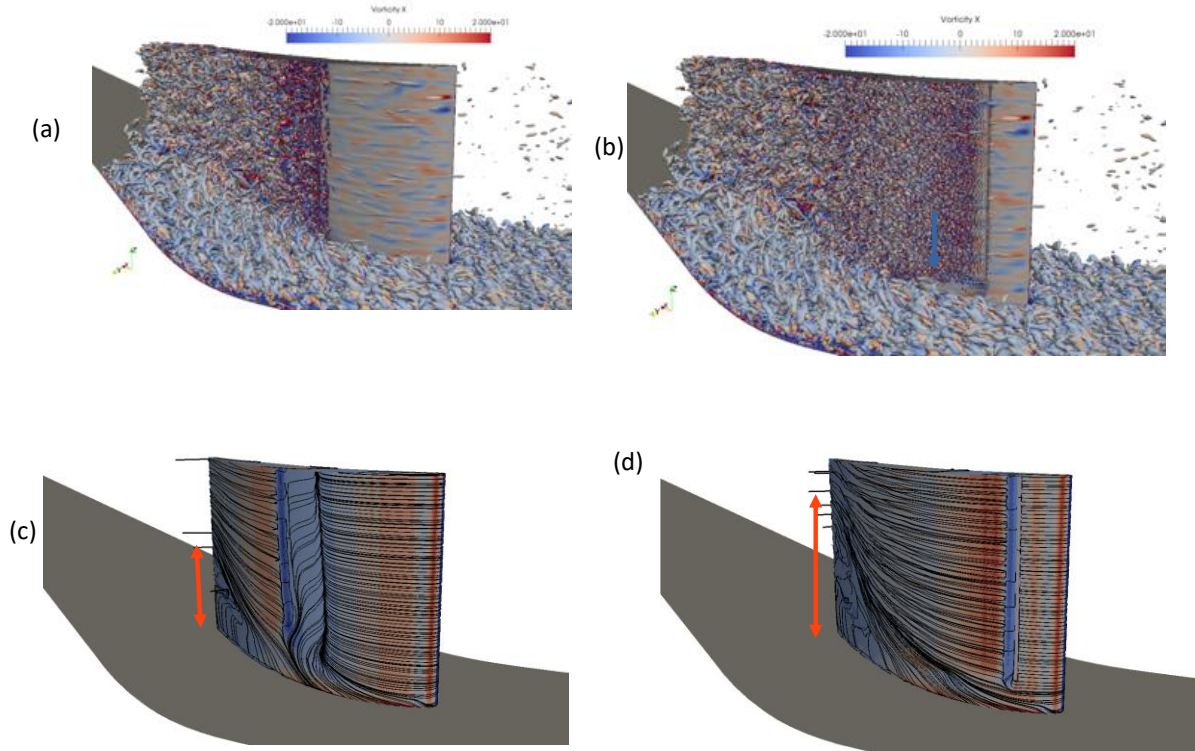


Figure 16. Impact of transition location on endwall flow blockage: (a) Instantaneous Q-criterion for un-tripped flow; (b) Instantaneous Q-criterion for tripped flow; (c) surface streamlines for un-tripped flow and (d) surface streamlines for tripped flow.

Next staying with the suction surface, we replicate the experiment of Goodhand and Miller [25] who placed a trip positioned at around 7% chord. Here, this trip is replicated by a numerical body force term. The mesh used has around 70 million points. Figure 16, Frame (a) gives instantaneous isosurfaces of Q-criterion coloured by vorticity, where the transition is around the mid chord. Frame (b) is the equivalent for when the trip is applied at around 7% chord from the leading edge. Frames (c) and (d) give time averaged surface flow streamlines with and without the trip, respectively. The increased blockage shown in Frame (d) is striking. The compression system comprises many rotor-stator pairs. For a high-speed compressor the pressure rise against mass flow characteristic curves for each of these are steep curves, in the sense that a small perturbation in mass flow rate produces a large variation in pressure ratio. This sensitivity propagates through the compressor stages where the other stages also show this sensitivity. Hence, transition location can again be seen to be important not just for efficiency but operability.

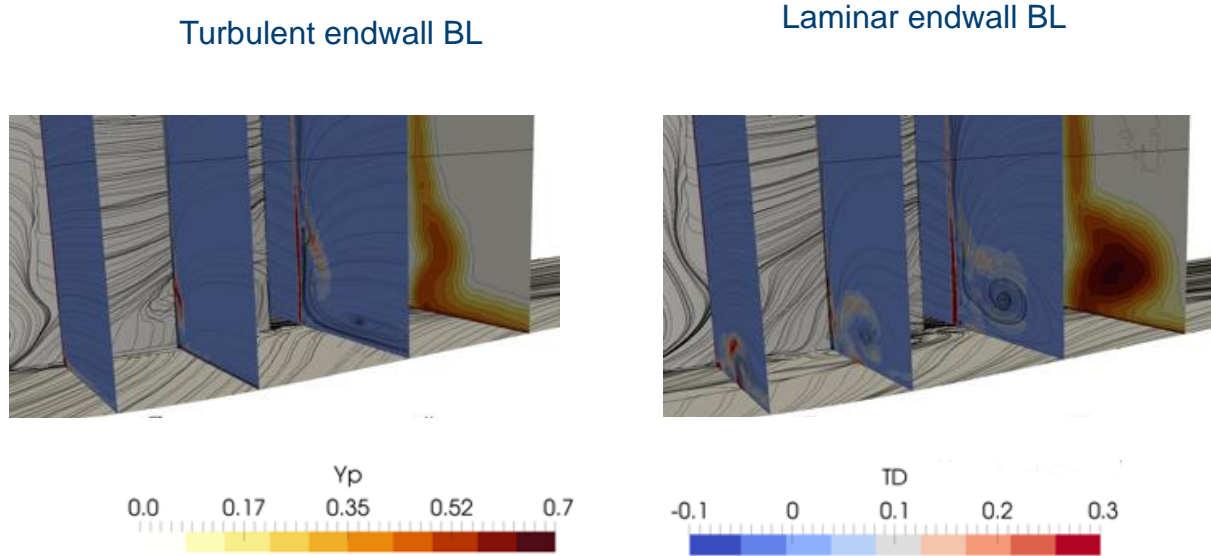


Figure 17. Contours of turbulent dissipation at three locations ($x/C_x = 0.41, 0.7, 1.1$) along with total pressure loss coefficient: left-hand frame turbulent endwall boundary layer and the right hand laminar endwall boundary layer (Adapted from Scillitoe et al. [26]).

State of Endwall Boundary Layer. The state of the endwall boundary layer is important. To elucidate this, contours of turbulent dissipation at three axial locations ($x/C_x = 0.41, 0.7, 1.1$, where C_x is axial chord) along with total pressure loss coefficient are presented in Figure 17. Full case details can be found in Scillitoe et al. [26]. The left-hand frame is for a turbulent endwall boundary layer and the right hand for a laminar endwall boundary layer.

The key difference is caused by the fact that the laminar endwall boundary layer cannot resist the adverse pressure gradient and so it separates much earlier. This leads to a much larger pressure leg of the horseshoe vortex which migrates down from the blade above, interacts with the corner separation and results in a large passage vortex giving a much larger downstream loss core. In many experimental campaigns the state of the endwall boundary layer is unknown. However, clearly the state of the endwall boundary layer has a strong impact on the compressor operation. Some of the issues discussed above can be found in the well resolved LES of Min et al. [27]

High-Pressure Compressor Drum

Air is taken from the compressor, addressed above, and ducted through the high-pressure compressor drum to cool hot components downstream of the combustor. These hot components will be discussed after we have dealt with the high-pressure compressor drum.

Note all simulations in this section use the NEAT computational fluid dynamics program. A popular, related, high pressure compressor drum flow is a system for generating atmospheric jet streams. This, as shown in Figure 18, consists of a rotating annular mass of fluid. This mass has an imposed radial temperature gradient. Depending on the gradient, angular velocity and fluid properties etc. an atmospheric jet stream is produced. This consists of a stream of fluid moving between cyclonic and anticyclonic vortices. For example, in Figure 18, there are three cyclones and three anticyclones.



Figure 18. Idealized atmospheric jet stream with three cyclones and three anticyclones (from Tucker [28])

This flow is interesting since it is reminiscent of that found in the high-pressure compressor drum to be discussed next and offers a useful code verification element.

Figure 19 contrasts experimental smoke flow visualization (Column (I)) with the numerical equivalent produced by solving a passive scalar equation for an idealized high-pressure compressor drum – see Column (II). Full case details can be found in Tucker [29]. The disc surface temperature distribution decreases with radius. This corresponds to an engine deceleration. This system produces one cyclone and anticyclone that flank a radial arm of fluid emanating from the axial throughflow. Rows (a) and (b) contrast the flow at two instants in time. From Row (a) the single radial arm flanked by cyclones and anti-cyclones is clear. The flow is largely unsteady. This is caused predominantly from a drift of the cyclone/anticyclone system relative to the cavity (just as occurs for the atmospheric jet stream). The flow topology, like that of the idealized atmospheric jet stream can take many forms depending on the flow parameters such as radial temperature gradient, angular velocity etc. Since the flow largely rotates at the cavity angular velocity except for a minor drift, the rotational Reynolds number of the flow relative to the cavity is modest. Hence, this flow is viewed as a Class B flow, as is the idealized atmospheric jet stream flow. However, for certain extremes in geometry and flow conditions this may not be true. Nonetheless, this geometry is a great challenge to RANS and the poor performance in such models when dealing with this flow is well documented. Notably, however, reliable detailed experimental data for the flow field is limited for this case.

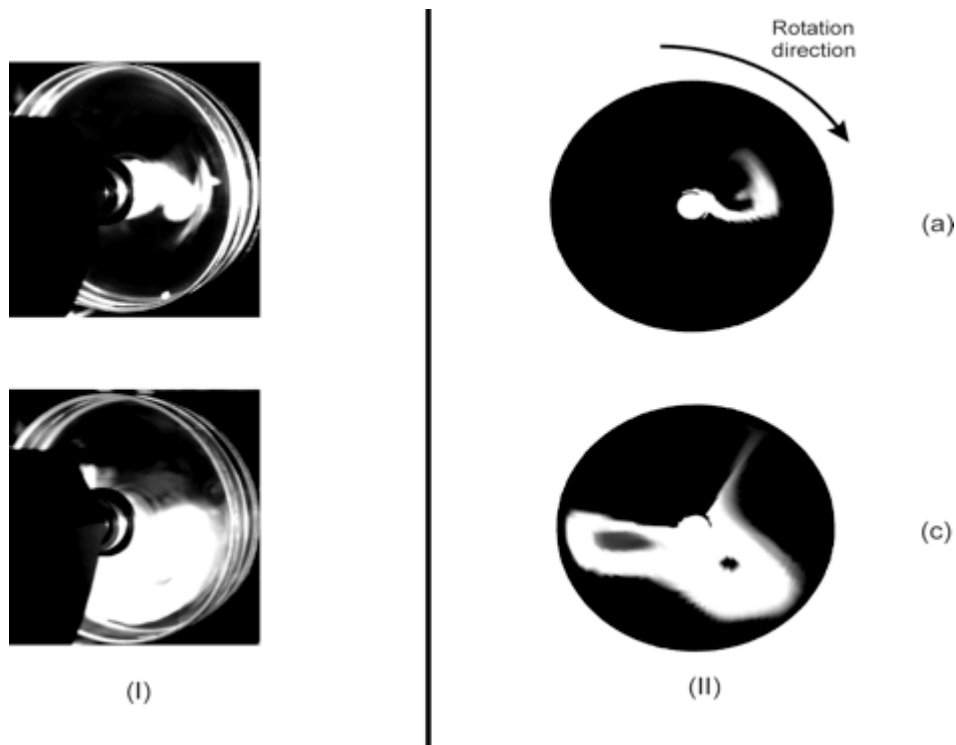


Figure 19. Flow structure in an idealized high-pressure compressor drum rendered visible using a passive scalar (Column (I) experimental flow visualization and Column (II) computations) – Adapted from Tucker [17].

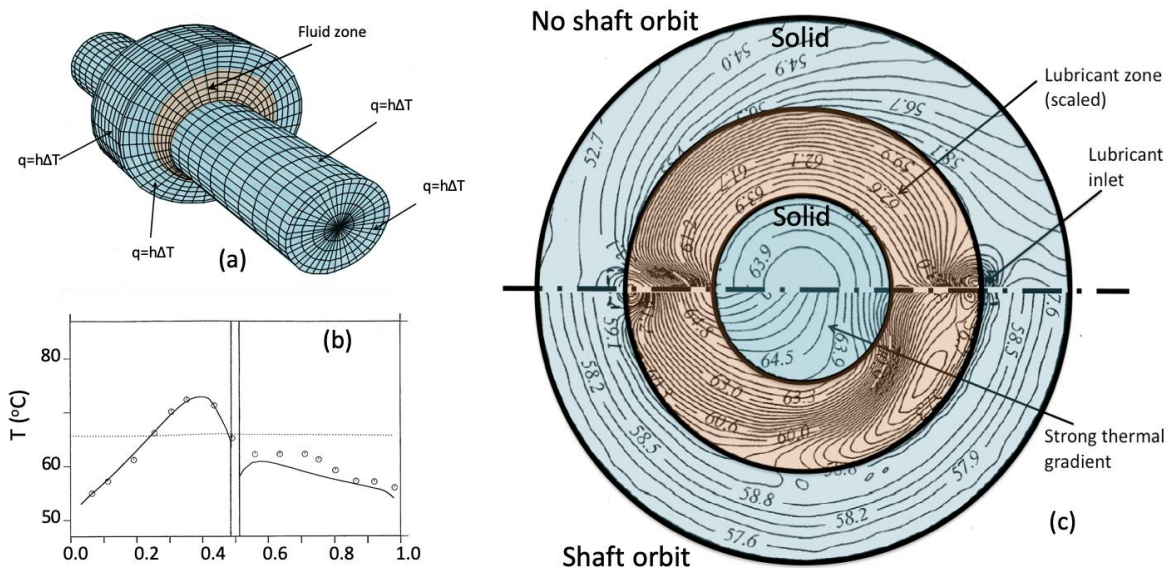


Figure 20. Hydrodynamic journal bearing with shaft orbit causing preferential heating, shaft bending and bearing failure: (a) conjugate mesh, (b) validation for when there is no orbit, (c) temperature distribution through the complete bearing when there is no shaft orbit (upper half) and when there is a shaft orbit (lower frame) - From Tucker [1], Published with the kind permission of Springer.

Note, the simulations in this section use the NEAT computational fluid dynamics program. Ground based turbines use hydrodynamic journal bearings. These have thin lubricant films and hence naturally small Reynolds numbers well below that of turbulence. However, when the shaft orbits higher Reynolds numbers can arise. The simulation considered here is motivated by the failure of a ground-based gas turbine. The failure was due to shaft orbiting causing preferential heating on a certain shaft area and hence shaft bending and bearing failure. Full test case details can be found in Tucker and Keogh [30]. The conjugate mesh is shown in Frame (a) of Figure 20. Frame (b) of this Figure gives validation for when there is no orbit. The plot shows the circumferential variation of bearing metal surface temperature. Symbols are the measurements and the line the prediction. As can be seen there is encouraging agreement. Notably, experimental data is very limited for these cases beyond surface quantity measurements. Frame (c) of Figure 20 gives the temperature distribution through the complete bearing when there is no shaft orbit (upper half) and when there is a shaft orbit (lower frame). The substantial radial temperature gradient with the shaft orbit is evident and this can give rise to turbine failure. Note, in Figure 20 the extent of the fluid zone is scaled to render it visible. Since this flow has extremely low Reynolds numbers it is considered here to be a Class B flow.

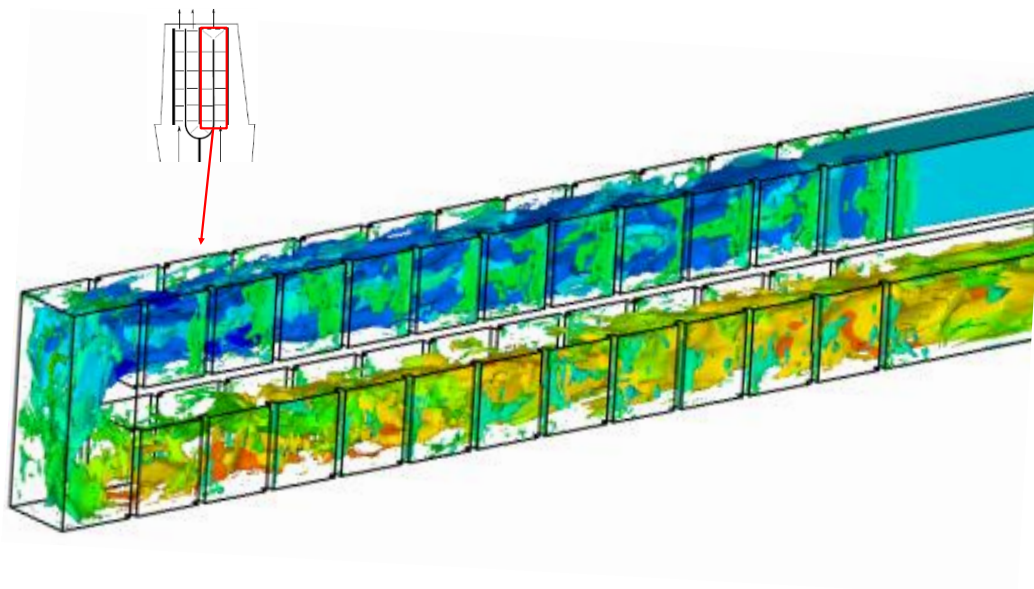


Figure 21. Flow in an idealized ribbed duct for cooling a high-pressure turbine (vorticity isosurfaces) – from Tyacke et al. [31].

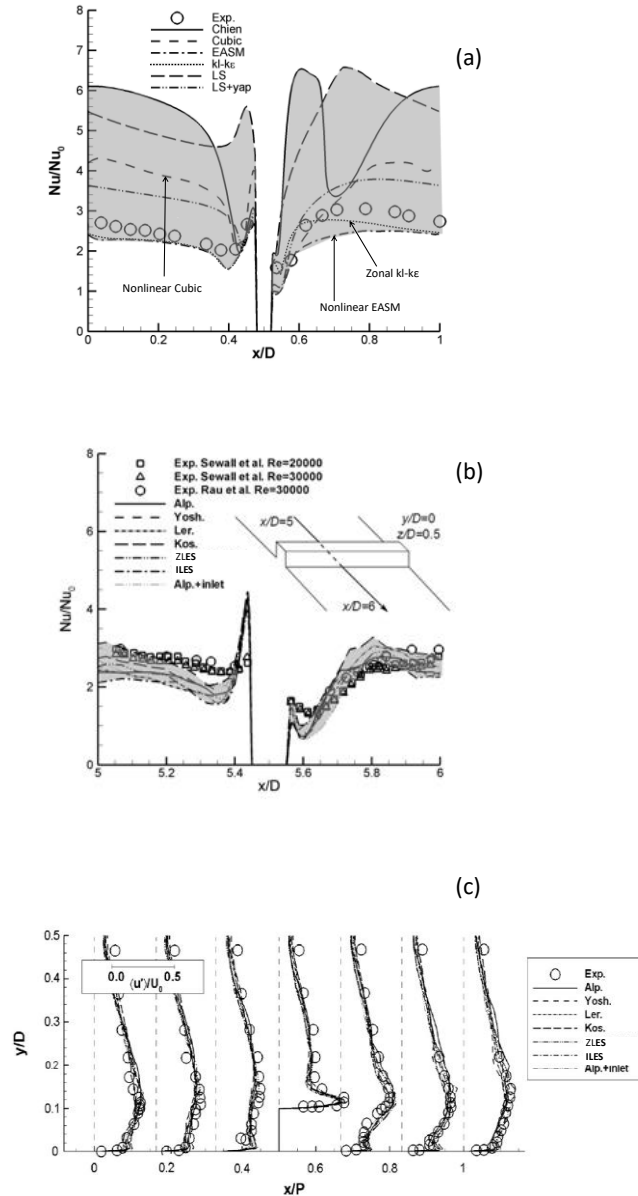


Figure 22. Inter-rib heat transfer and Reynolds stress distributions: (a) RANS heat transfer for different models; (b) heat transfer from LES for a range of LES methodologies and (c) streamwise Reynolds stress distribution - From Tyacke and Tucker [32].

Turbine Cooling

Ribbed Passages. Note all simulations in this section use the NEAT computational fluid dynamics program. The high-pressure turbine has internal cooling passages as shown in Figure 21. These have essentially wake type flows with Reynolds number independence i.e. Class A flows. It comes as no surprise that RANS models do poorly for this type of flow. See, for example, Frame (a), Figure 22 where the shaded zone shows the large scatter in RANS predictions. Note, the RANS models involve various $k-\varepsilon$ forms with differing near wall treatments, an explicit algebraic stress and also cubic model along with the Spalart-Allmaras model. The best heat transfer prediction is the the crudest model – the single equation linear Spalart-Allmaras model. On the other hand, as Frame (b) shows, LES does well for this type of flow. The frame shows results for four different subgrid scale models, no subgrid scale

model, ZLES and inlet turbulence versus no inlet turbulence. Despite the wide range of eddy resolving strategies used, the heat transfer results are consistent. Notably the RANS layer made little difference for this type of flow which is dominated by large eddies and has very little classical boundary layer content. Frame (c) shows predictions of streamwise Reynolds stress for the different eddy resolving strategies. As would be expected the results are all accurate and hence consistent. This is for a fairly coarse mesh $\sim 7M$ – even so the eddy resolving results show little sensitivity even for much coarser grids. Full test case details can be found in Tyacke et al. [33].

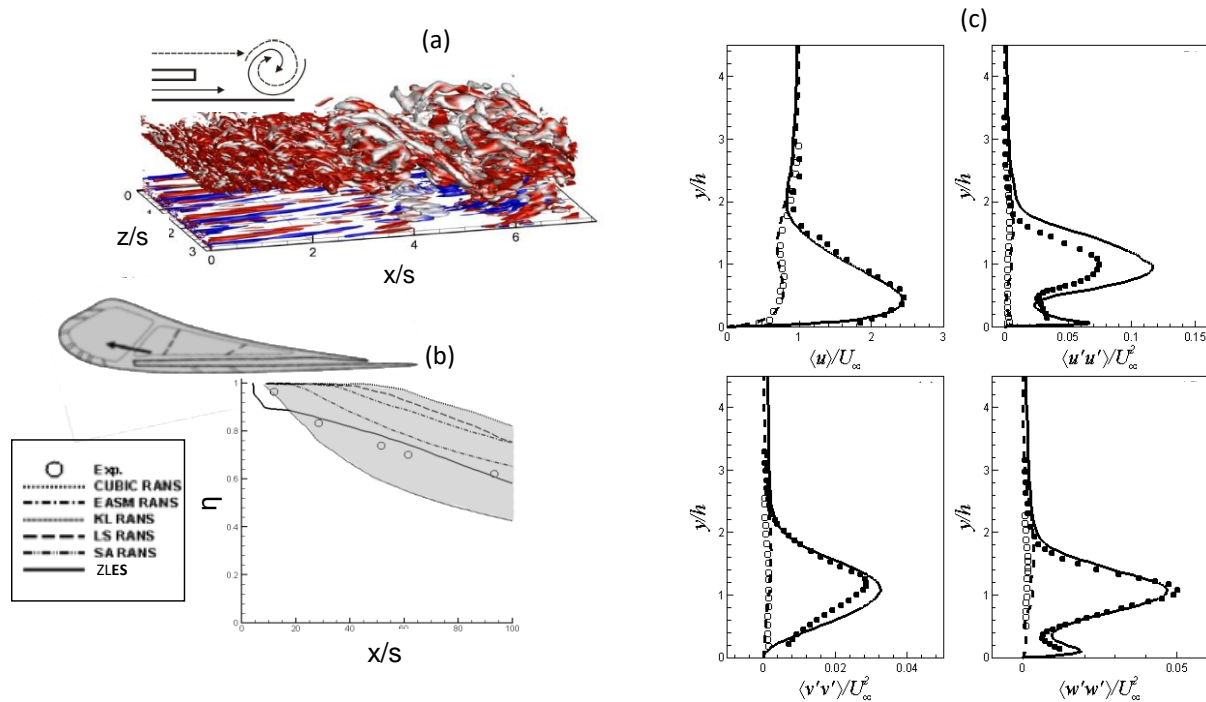


Figure 23. Performance of eddy resolving simulations for a cut back trailing edge: (a) instantaneous flow structure (Q criterion); (b) adiabatic film cooling effectiveness and (c) velocity and Reynolds stress profiles – from Tyacke et al. [31].

Cut Back Trailing Edges. Figure 23 shows some comparisons with the measurements of Kacker and Whitelaw [34] for an idealized cut back trailing edge. The trailing edges are idealized largely in the sense that they are not populated with the internal pins connecting the pressure to the suction surface of the blade. Therefore the RANS layer is just applied along the lower wall i.e. the focus zone for the heat transfer. Frame (a) shows the flow structure characterized by instantaneous isosurfaces of Q criterion. Frame (b) shows the adiabatic film cooling effectiveness. There is again a notable scatter between the results for the RANS simulations. Again, the Spalart-Allmaras model is closest to the measurements. However, the use of this RANS would steer a design optimization in the wrong direction (i.e. not even getting the sign of changes correct). The ZLES gives much more encouraging results. This adiabatic film cooling effectiveness quantifies how well the thin blade trailing edge is shielded from the hot gasses. A film cooling effectiveness of unity would mean perfect shielding from hot air by the cooler fluid directed through the blade. Frame (c) gives cross stream distributions of mean velocity and Reynolds stresses. Comparison is made with hot wire measurements, given by the symbols. The open symbols represent $r = 0.75$ and the shaded symbols are for $r = 2.3$ where r

is the ratio of the film cooling to the free stream velocity. The profiles are shown at 10 film cooling flow vertical widths downstream from the film cooling exit.

Motivated by these encouraging results and also those of Martini et al. [35], for this notionally Class A (more so when the internal wake inducing pins are included), flow Watson and Tucker [36] optimized internal geometry for adiabatic cooling effectiveness. The optimization involved over 600 ZLES simulations for different internal pin layouts and was genetic algorithm based. This genetic algorithm framework is highly parallel. Numerous jobs can be run in parallel and each job is also naturally spread across many processors. Hence, this approach is well suited to eddy resolving simulation strategies.

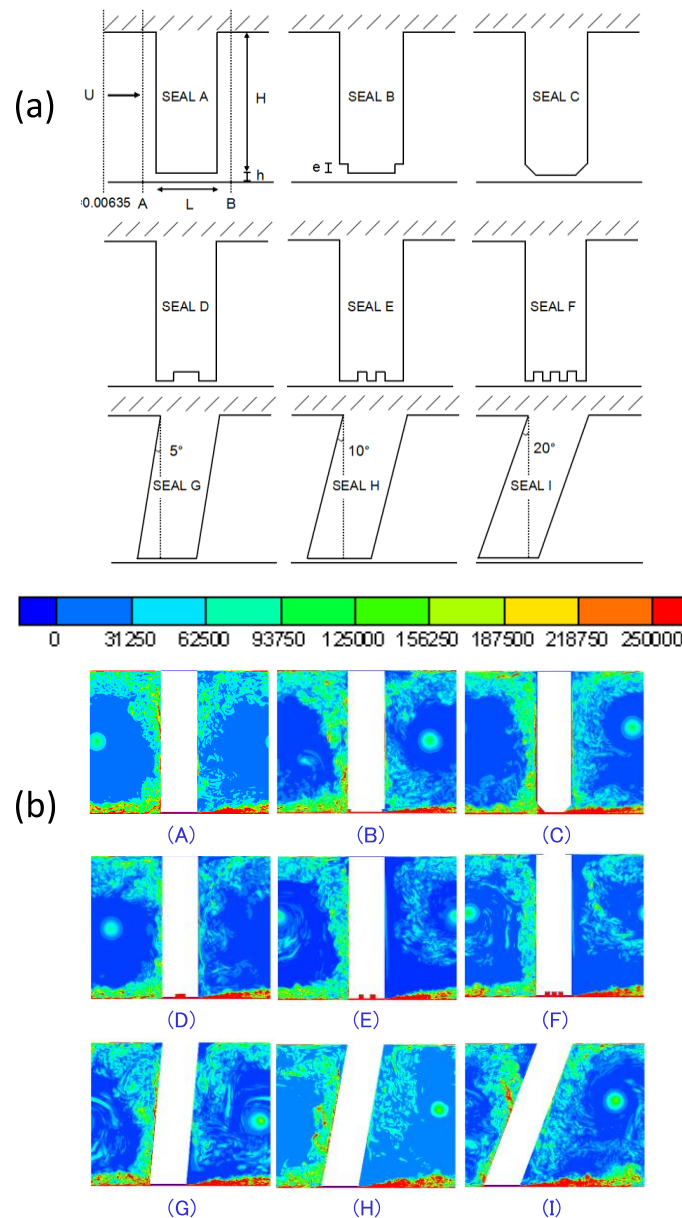


Figure 24. Genetic algorithm based optimization of a labyrinth seal: (a) Sample geometries and (b) corresponding contours of instantaneous vorticity magnitude.

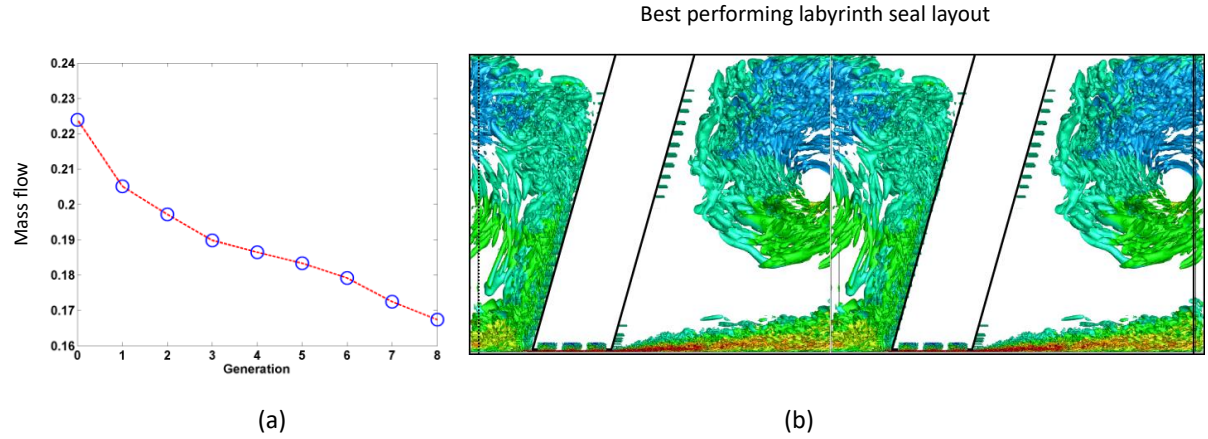


Figure 25. Path of mass flow to best design and flow for the best design: (a) variation of mass flow with generation and isosurfaces of Q-criterion for the best design.

Labyrinth Seals

The initial simulations in this section use the NEAT computational fluid dynamics program. Inspired by the work of Watson and Tucker [36], Dai et al. [37] perform a well-resolved (average grid spacings around 10 in wall units) LES based optimization of labyrinth seals with the α subgrid scale model (Domaradzki, and Holm [38]). The IBM method was used to facilitate rapid geometry changes that avoided remeshing. Well over 300 seal geometries were explored in a genetic algorithm-based optimization. Figure 24, upper images, gives a small sample of the geometries explored. The lower images give contours of instantaneous vorticity magnitude for these geometries. Notably, honeycombing was also explored in the work of Dai [39], this being an important element in seal designs. Figure 25(a) shows the reduction in mass flow rate, for a fixed pressure difference across the seal, against generation, in the genetic algorithm based optimization. Clearly a substantial improvement has been made. Finally, Frame (b) of Figure 25, gives instantaneous isosurfaces of Q criterion for the best performing design. This involved sloped seals with grooves at the seal tips.

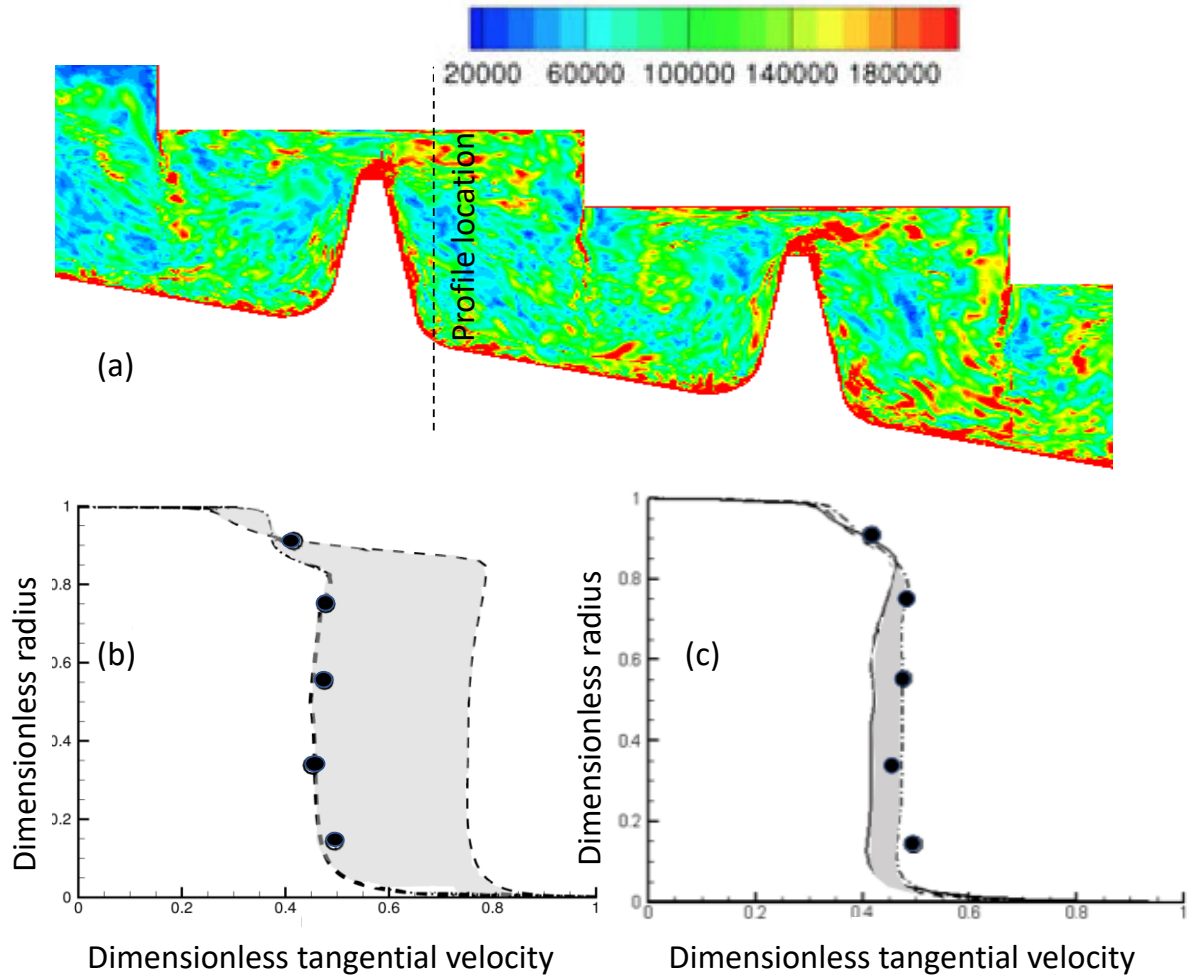


Figure 26. Swirl distribution in a labyrinth seal: (a) Instantaneous flow contours of vorticity magnitude; (b) Scatter in swirl velocity for a range of RANS models and (c) Scatter for a ZLES and two LES approaches.

Figure 26 looks further at labyrinth seals but for a different design with a swirl velocity component. Full case details can be found in Tyacke et al. [40]. Frame (a) gives instantaneous contours of vorticity magnitude. Frame (b) shows the scatter in swirl velocity for a range of RANS models. The RANS models include the $k-\varepsilon$ (RNG), a Reynolds stress model and three implementations of the Menter SST model in different codes. The largest discrepancy, this time, is between different codes. This makes it even harder to judge the best RANS model to use ahead of having data. Note the scatter is identified by the grey shaded zone and the individual curves are not needlessly reproduced. Frame (c) shows the scatter for a ZLES and two other LES approaches (Germano model and a transport equation for subgrid scale kinetic energy). The scatter is now considerably lower. Hence, even though this is a Class D flow, results can be achieved using relatively modest meshes of around 10 m cells (resolving four seal teeth) using ZLES and also LES. Perhaps the large outer flow scales dilute the need for capturing well, the streak structures generated by the high tangential velocity components.

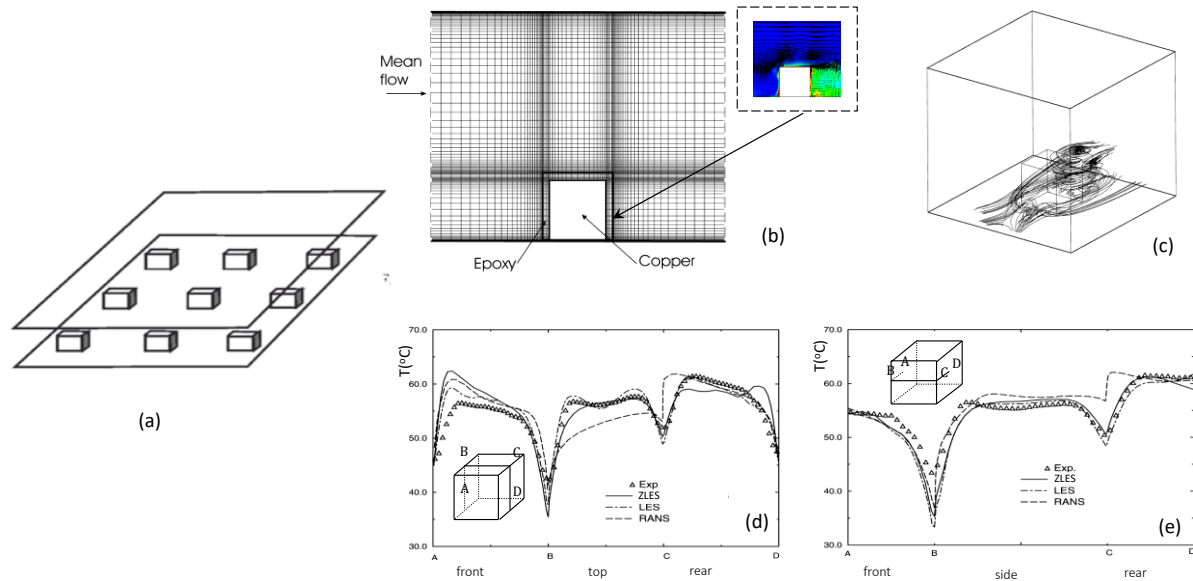


Figure 27. Idealization of an array of integrated circuits on a circuit board: (a) geometry; (b) mesh; (c) time averaged streamlines and (d,e) cube surface temperatures – From Tucker [1], Published with the kind permission of Springer.

Avionics

Note, simulations in this section use the NEAT computational fluid dynamics program. Avionics is a critical element of modern gas turbines and are necessary for stabilizing the engine. Figure 27, Frame (a) represents an idealization to an array of Integrated Circuits (ICs) on a (circuit) board. The ICs are idealized as a copper core with an outer epoxy layer. The simulations are bi-periodic and conjugate. Frame (b) shows the mesh distribution. Frame (c) gives time averaged streamlines that clearly identify the wake region. Frames (d,e) give cube surface temperatures along the lines indicated in the insets of the graphs. ZLES (full line), LES (chain dashed line) and $k-\varepsilon$ RANS (dashed line) simulations are made. The LES used a 1.3 million cell grid and the ZLES just under 0.5 million cells. As would be expected the LES for this Class A flow does best. The near wall RANS model in the ZLES appears to dilute accuracy. The RANS results have the most obvious defects. Full case details can be found in Zhong and Tucker [41].

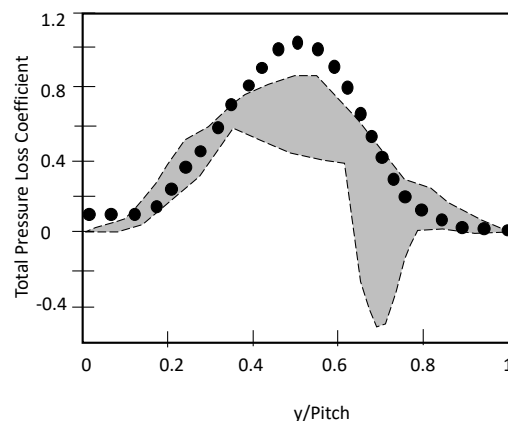


Figure 28. Total pressure loss in wake of a low-pressure turbine blade (symbols are measurements and the grey shaded area the scatter in RANS predictions) – based on Arko and McQuilling [42].

Turbine Blades

Mid-Span. Next we move to the low-pressure turbine. This can be responsible for around 80% of the engine's thrust. With regards to RANS error, Arko and McQuilling [42], show the local total pressure loss coefficient can be 100% or more in error depending on the RANS model choice when predicting low pressure turbine flows. Figure 28 shows this RANS model scatter using the grey shaded zone. The measurements are represented by symbols. The results here will focus on the well-known T106A high lift, cascade, profile having $Re_c = 1.6 \times 10^5$.

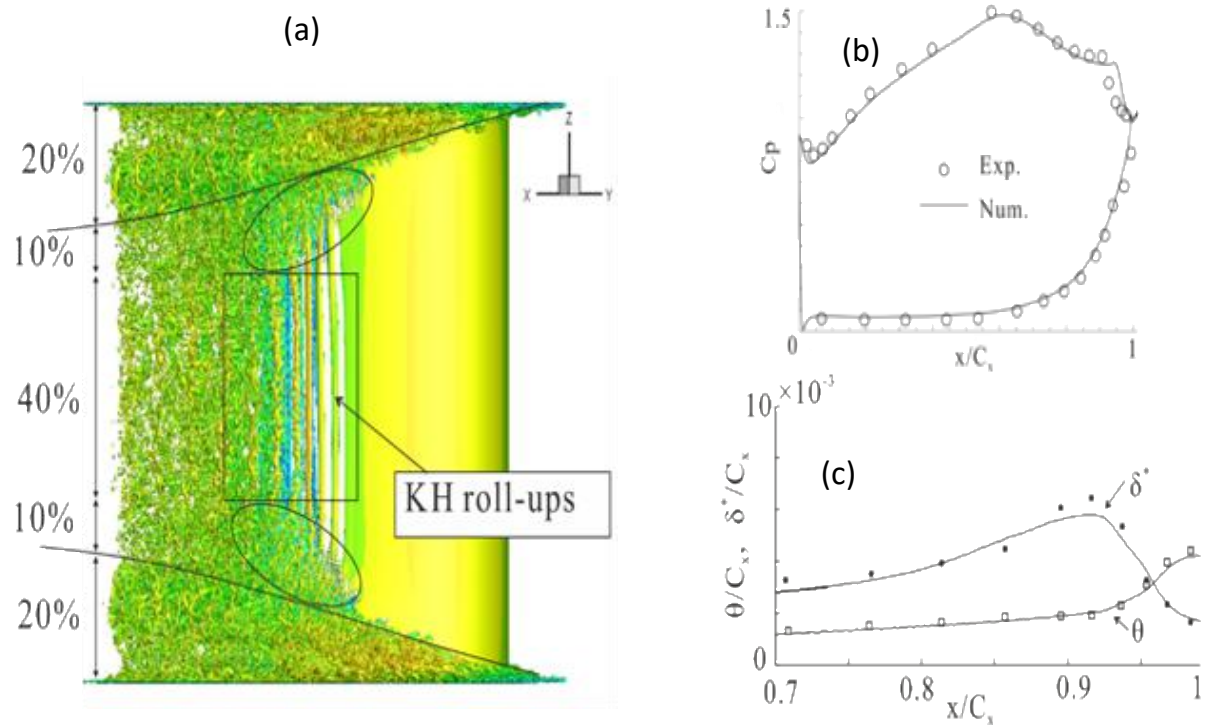


Figure 29. Flow, pressure coefficient, momentum and displacement thickness distributions for a low pressure turbine: (a) instantaneous flow for the full span; (b) C_p predictions (full line) & measurements (symbols) at the midspan and (c) development of the momentum and displacement thickness along the suction surface – From Cui and Tucker [45].

This is a relatively easy Class B flow and there have been successful DNS for just the midspan of this case for around two decades (see, for example, Wu et al. [43]). Figure 29 shows the low-pressure turbine LES results from Cui et al. [44]. Frame (a) shows the flow for the full span case. Frame (b) compares the C_p predictions (full line) with measurements (symbols) at the midspan. Similarly, Frame (c) show the development of the momentum and displacement thickness along the suction surface. For all comparisons there is encouraging agreement. Although not shown here, there is also encouraging agreement for both low and high levels of free stream turbulence intensity for the quantities already shown, along with the time variation of momentum thickness at the suction surface trailing edge (see Cui et al. [44]).

Importantly, the simulations also show a similar transition mechanism to that shown for the compressor i.e. that the wakes impinging on the leading-edge result in intensified Klebanoff streaks. These convect at around 70% of the free stream velocity, ultimately directly interacting

with the separated shear layer on the suction surface and causing transition. Hence, again this is a challenge for existing RANS models.

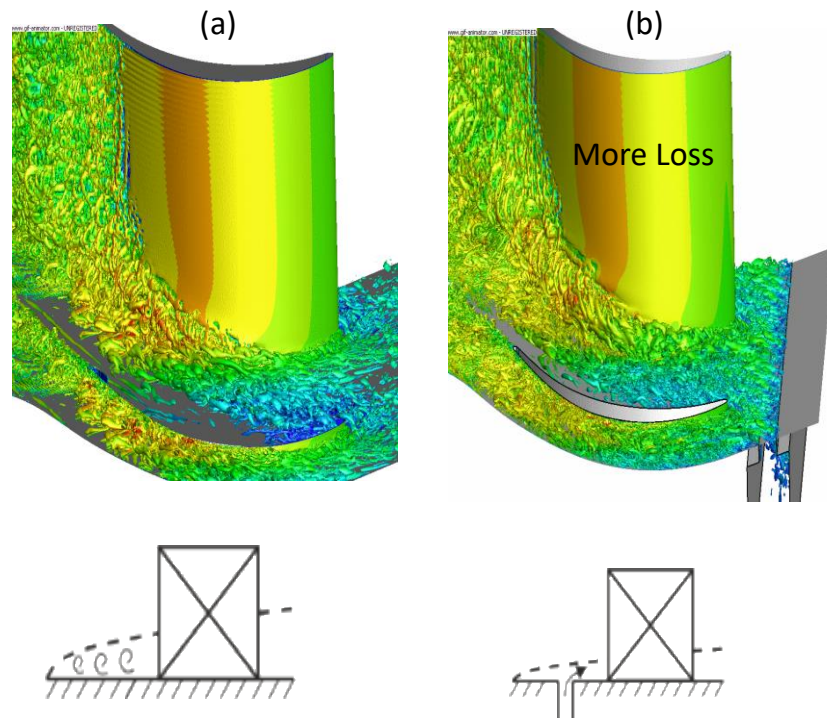


Figure 30. Comparison of flow when the endwall is clean and when there is a purge flow: (a) clean endwall and (b) purge flow included – From Cui and Tucker [45].

Real Geometry Features. Cui et al. [45] explore the impact of purge flows on LPT loss - see Figure 30. Frame (a) shows the T106A profile with an endwall boundary layer and Frame (b) with a purge flow. The latter is shown by Cui et al. to give around 10% more loss. Note, Tucker [1] finds 25% more loss for a high-pressure turbine when performing ZLES for this challenging Class D flow.

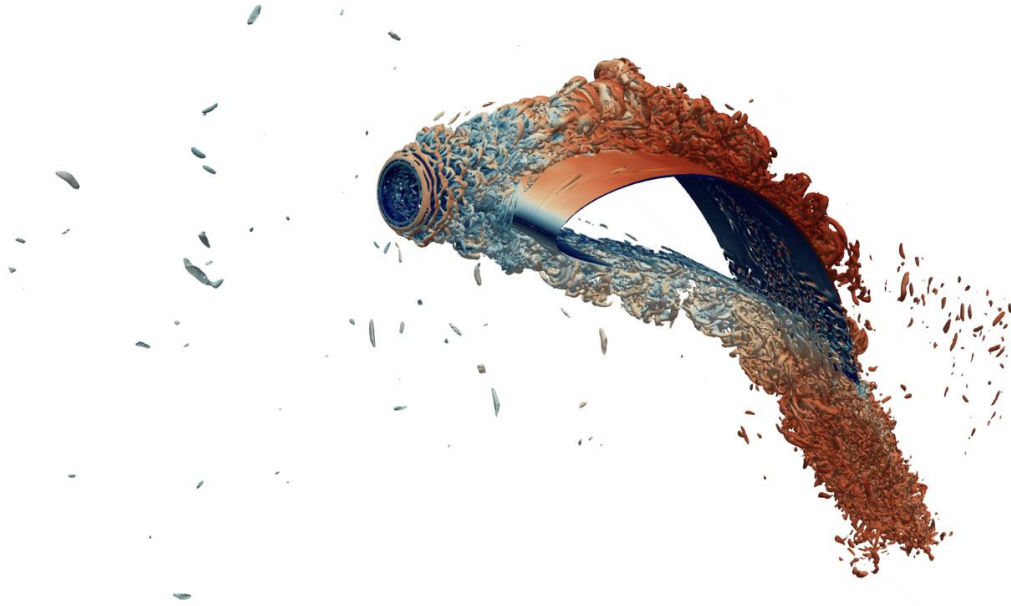


Figure 31. Flow over an LPT profile with leading edge instrumentation.

Looking at real geometry features further, Ubald et al. [46] looked at the impact of leading-edge instrumentation and the substantial loss that this causes. This is clear from the Q-criterion isosurfaces for the instantaneous flow show in Figure 31. Notably, in this figure the IBM method is used to resolve the probe geometry, the blade surface being fully mesh resolved. Much of the probe has DNS grid resolution with LES over the blade surface.

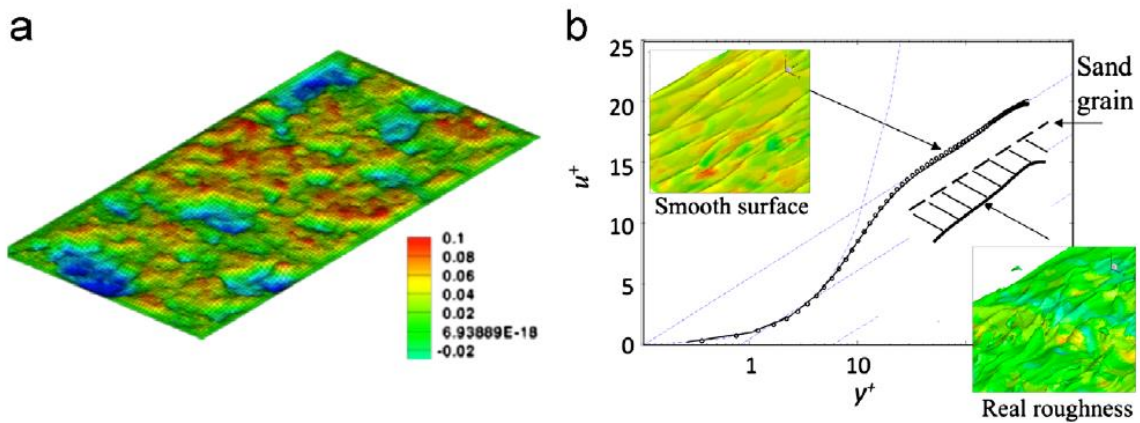
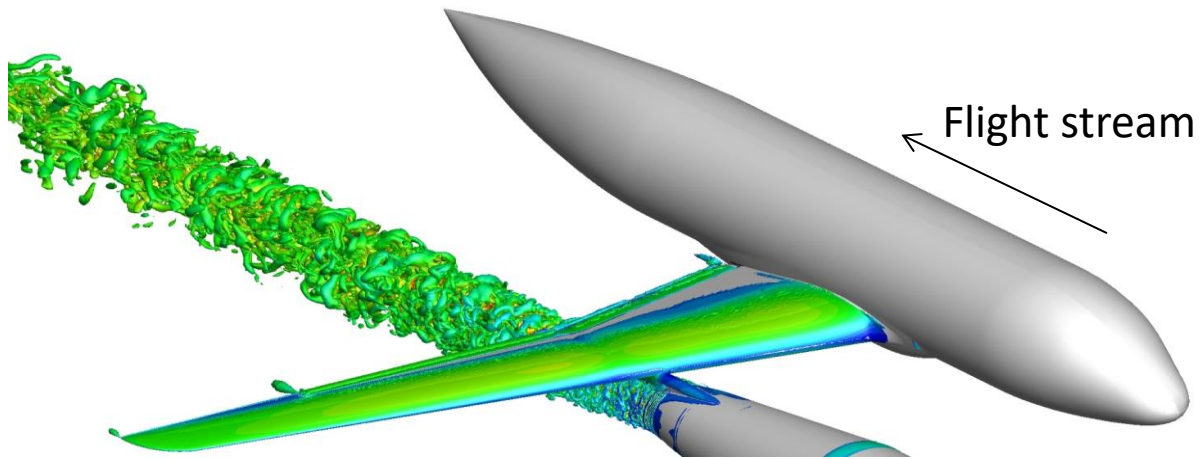


Figure 32. Real roughness in a high-pressure turbine: (a) real roughness scan from a high pressure turbine and (b) the law of the wall from DNS – From Tucker [51],fig 14.

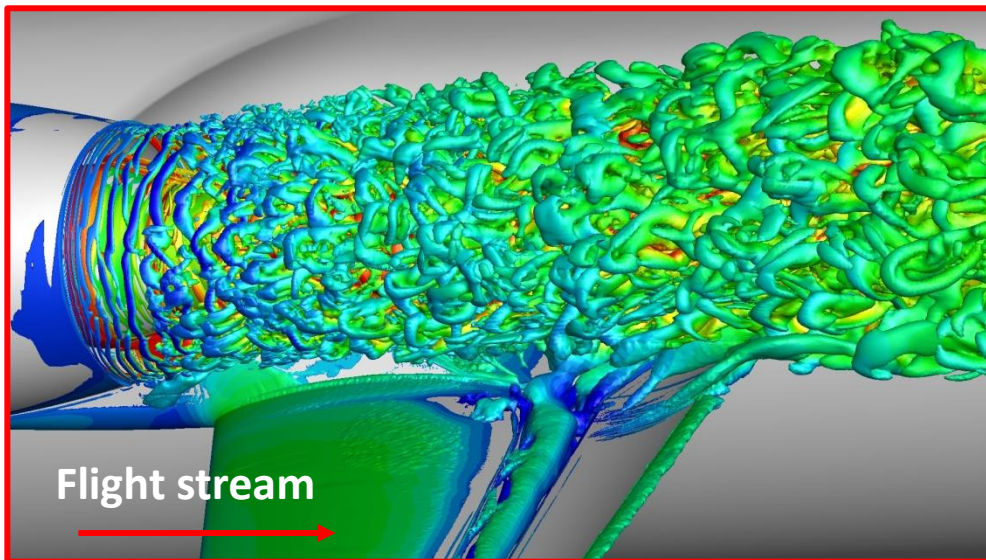
Staying with real geometry features, Yang [47] took a real roughness scan from a high-pressure turbine and found 80% more skin friction. The form of the roughness can be seen from Frame (a) of Figure 32. Frame (b) shows the law of the wall from the DNS of Yang [33]. The symbols represent a reference DNS and the line Yang's replication of this for

validation. The dashed line is for a sand grain roughness (when the root mean square for roughness height for the real roughness is put into Ligrani and Moffat's [48] correlation for sand grain roughness). The lower, thicker line, is the result for real roughness. An alternative approach for analyzing roughness in compressor and turbines is to use equivalent discrete roughness [49,50].

These real geometry features amongst others would explain why when predicting the mass flow rate through the engine the Computational Fluid Dynamics (that does not typically contain these features) gives a higher mass flow rate.



(a)



(b)

Figure 33. Installed jet noise: (a) Global view of Q-criterion isosurfaces and (b) low view.

Installed Jets

Isolated jets give a Class A flow. With ever increasing bypass ratios it is now becoming especially important to understand the aerodynamic and aeroacoustic interactions between the propulsive jet and the airframe. The airframe presents some Class D elements. Hence, such problems could be classed as Class A/D. However, at the jet-airframe interaction zones that are of critical importance the boundary layer content is likely to be diluted by the powerful jet. Hence, the flow might lean more to Class A. This can perhaps be seen in a global sense in Figure 33a, where Frame (b) gives a zoomed in view of this interaction.

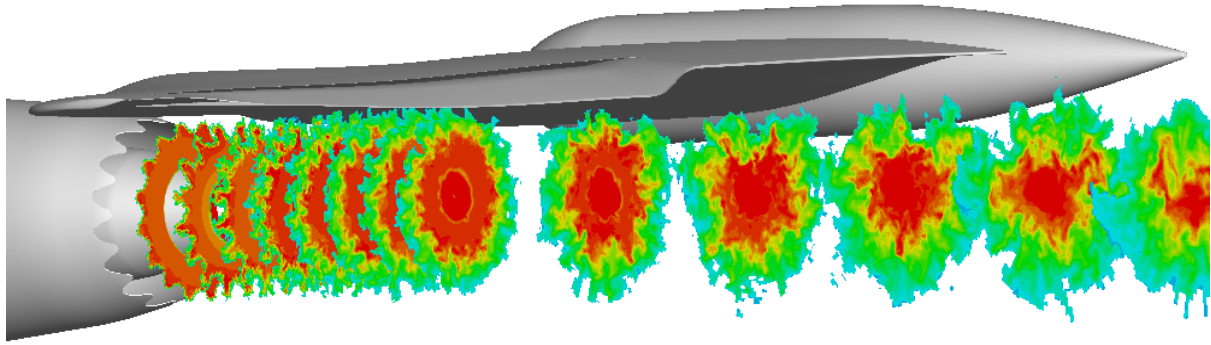


Figure 34. Installed jet noise with chevrons

Chevrons (serrations) are nowadays frequently employed to mitigate noise. Hence, as shown in Figure 34, eddy resolving simulations of this type are also emerging (see, for example, Wang et al. [52]) and these show the potential noise reductions when exploiting chevrons on installed jets. Such simulations clearly show (see Wang et al.) that the chevron breaks up large scales, in the jet shear layer, putting energy into smaller scales. The latter becomes relatively quickly weakened prior to interacting with the downstream airframe resulting in less sound.

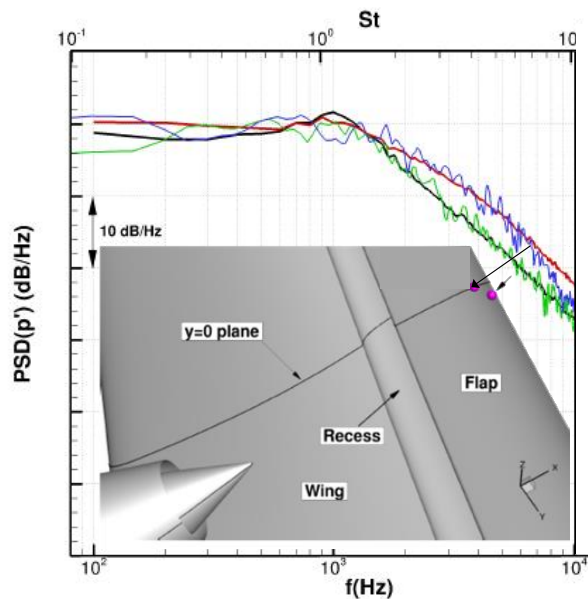


Figure 35. Locations of unsteady pressure probes and power spectral density for unsteady pressure probes.

The Figure 35 inset, indicates the location of unsteady pressure probes on the flap pressure surface when the chevrons are omitted. Surface pressure spectra for these locations are shown in Figure 35 and compared with measurements. There is close agreement between the ZLES and the measurements. This is an important aspect, as the flap trailing edge is responsible for a large portion of the installed noise sources. The flap chord and local convective speed correspond to 1200 Hz. Higher frequencies are generated by the jet shear layer. Lower frequencies relate to largescale interaction effects (see Tyacke et al. [53]). Figure 36 shows the complex acoustic interference patterns (rendered visible from contouring instantaneous density gradients) that arise from interactions with different components.

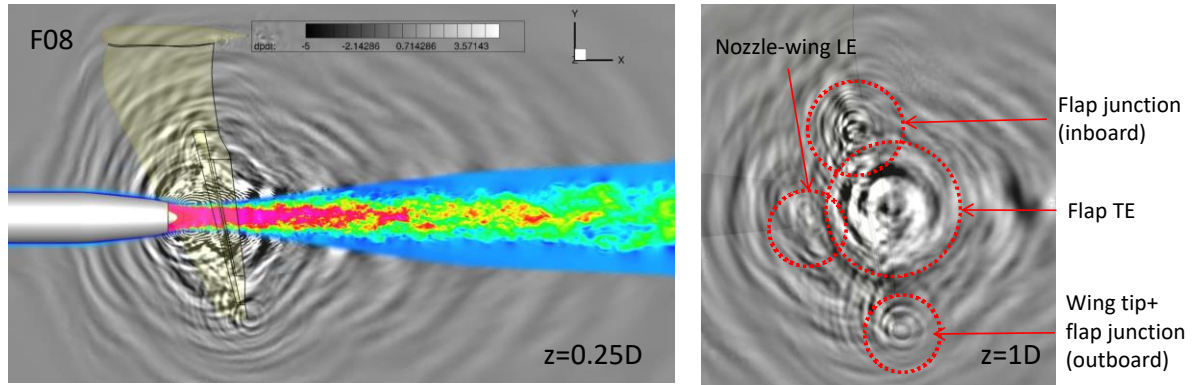


Figure 36. Complex acoustic interference patterns that arise from interactions with different components – From Tyacke et al. [53].

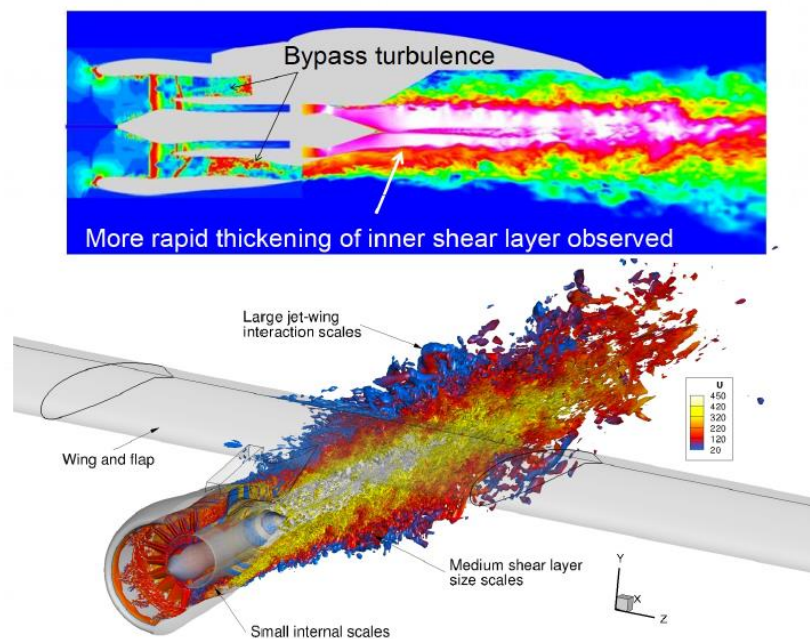


Figure 37. Hybrid, hierarchical simulation of flow from the fan to a deployed flap – From Tyacke et al. [54].

Negating the increased nacelle wetted area has given rise to the shortening of the engine and a drive towards thinning the intake lip (nacelle). This worsens the incidence tolerance on the nacelle lip. This shortening also increases the axial coupling between the numerous rotating and stationary components and also the coupling between the engine, the intake and any separated flow there. The increased fan diameter creates coupling between the engine and airframe, notably wings and flaps. This coupling is further controlled by the engine's intake flow and the development of this through the engine (primarily the engine bypass duct). This development impacts on the global spreading of the propulsive jet and hence how it will interact with the airframe. The simulation shown in Figure 37 attempts to replicate this coupling. In this, the flow entering the intake of a high bypass ratio commercial engine is considered

mounted, via a pylon to a wing. Figure 37 shows a ZLES of this case from Tyacke et al. [54] & Tucker [1]. The fan and outlet guide vanes (and their wakes) are modelled using a hybridization of IBMfg and a low order IBM related approach. This IBM approach is also used to model the A-frame and gearbox shaft found in the bypass duct. These components will generate additional turbulence. Full details of these simulations can be found in Tyacke et al. along with results validation for mean velocity profiles and Reynolds stresses. For the jet development the potential core is shifted around one jet diameter upstream (relative to the case with no upstream turbomachinery) – quantitative results not shown here (see Tyacke et al.).

Conclusions

The successful application of eddy resolving simulations to most areas (ignoring the combustor, for example) of a modern gas turbine aeroengine is considered. A coherent modelling framework is presented to address coupling challenges. The results are promising but many challenges remain. In the short term the use of eddy resolving simulations should see greater use in RANS + lower order model calibration/development – this is starting to happen already. Ideally RANS, LES & test should work in harmony. Currently certain costly engineering design problems can be avoided using scale resolving simulations or understood. The simulations presented are generally complex to setup. Whereas there is an ERCOFTAC Best Practice for RANS there is none for LES. Also, since the techniques used for LES of the individual cases are so specialized it would make sense to have Best Practices customized to each different turbomachinery component. Although it has been attempted to classify different turbomachinery flows, their very different physics makes this hard. Clearly the Class A (physically Reynolds number independent but not numerically) present a more modest LES challenge followed by the Class B flows. The class C and D flows generally present more severe challenges but even here there appear to be potential exceptions. For example, labyrinth seals appear tractable and also for fans, with near all modelling and strong RANS zonalization some fans might be amenable to simulation at affordable costs. Modern unstructured, high order methods appear as a promising means of lessening severe resolution requirements,

References

1. Tucker P. G. 2013. Unsteady computational fluid dynamics in aeronautics, Springer, ISBN 978-94-007-7048-5.
2. de Laborderie J., Duchaine F. and Gicquel L. 2017, Analysis of a high-pressure multistage axial compressor at off-design conditions with coarse large eddy simulation, 12nd European Conference on Turbomachinery Fluid Dynamics & Thermodynamics, Stockholm, Sweden, April, 2017, ETC Paper ETC2017-125.
3. de Laorderie J., Duchaine F., Vermorel O., Gicquel L. and Moreau S. 2016, Application of an overset grid method to the large eddy simulation of a high-speed multistage axial compressor, 61st ASME Turbo EXPO, Seoul, Korea, June, 2016, ASME Paper GT2016-56344.
4. de Laorderie J., Duchaine F., Vermorel O., Gicquel L. and Moreau S. 2020, Wall-modeled large-eddy simulations of a multistage high-pressure compressor, Flow, Turbulence and Combustion, 104, pp. 725-751.
5. Cao T., Hield P. and Tucker P.G. 2017. Hierarchical immersed boundary method with smeared geometry. AIAA Journal of Propulsion and Power, doi: 10.2514/1.B36190.
6. Tucker P. G., Eastwood S., Klostermeier C., Jefferson-Loveday R., Tyacke J. and Liu Y. 2011. Hybrid LES approach for practical turbomachinery flows: Part 1 - hierarchy and example simulations, ASME J. Turbomachinery, Vol. 134, No. 2, pg 021023 (10 pages).

7. Mayle R., 1991. The role of laminar-turbulent transition in gas turbine engines. ASME Trans. J. Turbomach.113, 509–537 (1991). ASME, International Gas Turbine and Aeroengine Congress and Exposition, 36th, Orlando, FL, 3–6 June 1991
8. Bhaskaran R., Jia F., Laskowski G. M., Wang Z. J. and Paliath U. 2017, Towards high-order large-eddy simulation of aero-thermal flows for turbomachinery applications, 62nd ASME Turbo EXPO, Charlotte, NC, June, 2017, ASME Paper GT2017-63358.
9. Lu Y., Liu K. and Dawes W. N. 2016, Fast high order large eddy simulations on many core computing systems for turbomachinery, 61st ASME Turbo EXPO, Seoul, Korea, June, 2016, ASME Paper GT2016-57468.
10. Cassinelli A., Montomoli F., Adami P. and Sherwin S. J. 2018, High fidelity spectral/HP element methods for turbomachinery, 63rd ASME Turbo EXPO, Oslo, Norway, June, 2018, ASME Paper GT2018-75733.
11. Garal A., Diosady L. T., Murman S. M. and Madavan N. K. 2016, DNS of low-pressure turbine cascade flows with elevated inflow turbulence using a Discontinuous-Galerkin spectra element method, 61st ASME Turbo EXPO, Seoul, Korea, June, 2016, ASME Paper GT2016-56700.
12. Marty J., Lantos N., Michel B. and Bonneou V. 2015, LES and hybrid RANS/LES simulations of turbomachinery flows using high order methods, 60st ASME Turbo EXPO, Montreal, Canada, June, 2015, ASME Paper GT2015-42134.
13. Oriji, U. R., Yang, X., and Tucker, P. G., 2014, Hybrid RANS/ILES for aero engine intake, Proceedings of ASME Turbo Expo 2014 GT2014 June 16-20, 2014, Dusseldorf, Germany, Paper No. GT2014-26472.
14. Crumpton, P. I., Moinier, P., and Giles, M. B., 1997, An Unstructured Algorithm for High Reynolds Number Flows on Highly Stretched Grids, Tenth International Conference on Numerical Methods for Laminar and Turbulent Flow, pp. 561–57
15. Rogers, S. E., Kwak, D., and Kiris, C., 1991, Steady and Unsteady Solutions of the Incompressible Navier-Stokes Equations, AIAA J., 29(4), pp. 603–610.
16. Spalart P., and Allmaras S., 1992, A One-Equation Turbulence Model for Aerodynamic Flows, In AIAA 92-0439, AIAA 30th Aerospace Sciences Meeting and Exhibit, Reno, NV, pp. 1–27.
17. Tucker P. G. 2001. Computation of unsteady internal flows, Springer, ISBN 978-1-4615-1439-8.
18. Oriji Ugochukwu R.. 2014. Numerical investigation of intake flows in crosswinds, D.Phil. Thesis, Department of Engineering, Cambridge University.
19. Kalsi H. S., Tucker P. G. 2018. Numerical modelling of shock wave boundary layer interactions in aero-engine intakes at incidence, Proc. ASME. 50985; Volume 1: Aircraft Engine; Fans and Blowers; Marine, V001T01A019.June 11, GT2018-75872, doi: 10.1115/GT2018-75872.
20. Kalsi H. S. 2018. Numerical Modelling of Shock Wave Boundary Layer Interactions in Aero-engine Intakes at Incidence, D.Phil. Thesis, Department of Engineering, Cambridge University.
21. Zaki, T. A., Wissink, J. G., Rodi, W., and Durbin, P. A., 2010. “Direct numerical simulations of transition in a compressor cascade: the influence of free-stream turbulence”. J. Fluid Mech., 665, Oct, pp. 57–98.
22. Scillitoe A., Tucker P. G. Adami P. 2019. Large eddy simulation of boundary layer transition mechanisms in a gas-turbine compressor cascade, J. Turbomach; Vol. 141. No. 6. pp. 061008 - 061008-10 doi: 10.1115/1.4042023.
23. Gbadebo, S. A., 2003. Three-Dimensional Separations in Compressors. PhD thesis, University of Cambridge.

24. Nicoud, F., Toda, H. B., Cabrit, O., Bose, S., and Lee, J., 2011. Using singular values to build a subgrid-scale model for large eddy simulations. *Phys. Fluids*, 23(8), pp. 085106 1–35.
25. Goodhand, M. N., and Miller, R. J., 2012, “The Impact of Real Geometries on Three-Dimensional Separations in Compressors,” *ASME J. Turbomach.*, 134(2), p. 021007.
26. Scillitoe A.D., Tucker P.G., Adami P. 2017. Numerical investigation of three-dimensional separation in an axial flow compressor: The influence of free-stream turbulence intensity and endwall boundary layer state, *J. of Turbomachinery*, Vol. 139, No 2, 021011 (Oct 26, 2016) (10 pages).
27. Min B.-Y., Joo J., Mendoza J., Lee J., Xia G. and Medic G, 2018, Large-eddy simulation of corner separation in a compressor cascade, 63rd ASME Turbo EXPO, Oslo, Norway, June, 2018, ASME Paper GT2018-77144.
28. Tucker P. G. 2016. *Advanced computational fluid and aerodynamics*, Cambridge University Press, ISBN: 9781107428836.
29. Tucker P. G. 2002. Temporal behaviour of flow in rotating cavities, *Numerical Heat Transfer*, 41(6-7), pp. 611-627.
30. Tucker P. G. and Keogh P. S. 1996. On the dynamic thermal state in a hydrodynamic bearing with a whirling journal using CFD techniques, *ASME J. Tribology*, 118(2), pp. 356-363.
31. Tyacke J., Tucker P. G., Jefferson-Loveday R. , Nagabhushana Rao V., Watson R., Naqavi I and Yang X., 2013 LES for turbines: methodologies, cost and future outlooks, *J. of Turbomachinery*, Vol. 136, No. 6, 061009 (Nov 9); DOI: 10.1115/1.4025589.
32. Tyacke, J. and Tucker P. G. 2015. Large eddy simulation of turbine internal cooling ducts, *Computers and Fluids*, Vol. 114, pp. 130-140.
33. Tyacke, J. and Tucker P. G. 2015. Large eddy simulation of turbine internal cooling ducts, *Computers and Fluids*, 114, pp. 130-140.
34. Kacker S. C. and Whitelaw J. H. 1971 The turbulence characteristics of two-dimensional wall-jet and wallwake flows. *J. Appl. Mech.* 38, 239.
35. Martini P., Schulz A., Bauer H.J., Whitney C. F., 2006. Film cooling effectiveness and heat transfer on the trailing edge cutback of gas turbine airfoils with various internal cooling designs. *J. Turbomach.* 128(1), 196–205
36. Watson R. and Tucker P. G., 2016. A perfectly parallel optimisation for cutback trailing edges, *AIAA J.* 54(7), pp. 2051-2060.
37. Dai Y., Tyacke J. and Tucker P. G. 2016 Effect of labyrinth seal configurations on leakage performance using LES, 54th AIAA Aerospace Sciences Meeting, AIAA Science and Technology Forum and Exposition, AIAA Paper No. AIAA-2016-2127.
38. Domaradzki J. A. and Holm D. D. 2001. Navier-Stokes-alpha model: LES equations with nonlinear dispersion, in *Modern Simulation Strategies for Turbulent Flow*, ed. by B.J. Geurts. ERCOFTAC Bulletin, 107 (Edwards, Ann Arbor, 2001)
39. Dai Y. 2018, *Large Eddy Simulation of Labyrinth Seals and Rib Shapes for Internal Cooling Passages*, D.Phil. Thesis, Department of Engineering, The University of Cambridge.
40. Tyacke. J., Jefferson-Loveday, R., Tucker, P. G., 2013, On the application of LES to seal geometries, *Flow Turbulence and Combustion*, 91, pp 827-848.
41. Zhong B. and Tucker P. G. 2004. k-l based hybrid LES/RANS approach and its application to heat transfer simulation, *International Journal for Numerical Methods in Fluids*, 46, October, pp. 983-1005.

42. Arko B. M. and McQuilling M. 2013. Computational Study of High-Lift Low-Pressure Turbine Cascade Aerodynamics at Low Reynolds Number, *AIAA Journal of Propulsion and Power*, 29(2) , pp. 446-459
43. Wu X, Jacobs R. G., Hunt J. C. R. and Durbin P. A. , 1999. Simulation of boundary layer transition induced by periodically passing wakes, *J. Fluid Mech.*, 398, pp. 109-153.
44. Cui J., Nagabhushana Rao V. and Tucker P. G., 2015. Numerical investigation of contrasting flow physics in different zones of a high-lift low pressure turbine blade, *Journal of Turbomachinery*, 138(83), 011003.
45. Cui J. and Tucker P.G. 2016. Numerical study of purge and secondary flows in a low pressure turbine, *J. of Turbomachinery*, 139(2), 021007 (Oct 04, 2016) (10 pages); doi: 10.1115/1.4034684.
46. Ubalde B. N., Tucker P. G., Cui J. Watson R. Shahpar S. 2019. Numerical analysis of an instrumented turbine blade cascade, *J. Turbomach.*, 14(5), pp. 051013-051013-9 , doi: 10.1115/1.4041935.
47. Yang. X. 2014. Numerical investigation of turbulent channel flow subject to surface roughness, acceleration, and streamline curvature, D.Phil. Thesis, Department of Engineering, Cambridge University.
48. Ligrani, P.M. & Moffat, R.J. 1986. Structure of transitionally rough and fully rough turbulent boundary layers. *Journal of Fluid Mechanics*, 162, pp. 69–98.
49. Joo J., Medic G. and Sharma O. P. 2017, Large-eddy simulation of roughened NACA65 compressor cascade, 62nd ASME Turbo EXPO, Charlotte, NC, June, 2017, ASME Paper GT2017-64889.
50. Joo J., Medic G. and Sharma O. P. 2016, Large-eddy simulation investigation of roughness on flow in a low-pressure turbine, 61st ASME Turbo EXPO, Seoul, Korea, June, 2016, ASME Paper GT2016-57912.
51. Tucker P. G. 2013. Trends in turbomachinery turbulence treatments, *Progress in Aerospace Sciences*, Vol. 63 (November 2013), pp. 1-32.
52. Wang Z.-N., Tyacke J. and Tucker P. G. 2017. LES-RANS of installed ultra-high bypass-ratio coaxial jet aeroacoustics with a finite span wing-flap geometry and flight stream - Part 2: chevron nozzle. 23rd AIAA/CEAS Aeroacoustics Conference, AIAA AVIATION Forum, AIAA Paper No. AIAA 2017-3855, 10.2514/6.2017-3855.
53. Tyacke J.C., Wang Z-N. and Tucker P.G. 2019. LES-RANS of installed ultra-high bypass-ratio coaxial jet aeroacoustics with flight stream, *AIAA J.*, 7(3), pp. 1215-1236, doi 10.2514/1.J05705.
54. Tyacke J. C., Mahak, M. and Tucker, P. G. 2016. Large scale, multi-fidelity, multi-physics, hybrid RANS-LES of an installed aeroengine, *AIAA J. Propulsion and Power*, Vol. 32, No. 4, pp. 1-12, March doi: 10.2514/1.B35947.